

Redox and Guest Tunable Spin-crossover Properties in a Polymeric Polyoxometalate

Mario Palacios-Corella,^a Víctor García-López,^a Joao Carlos Waerenborgh,^b Bruno J. C. Vieira,^b Guillermo Mínguez Espallargas,^a Miguel Clemente-León^{*a} and Eugenio Coronado^{*a}

^a Instituto de Ciencia Molecular (ICMol), Universitat de València, C/ Catedrático José Beltrán 2, 46980 Paterna, Spain. Fax: 34 963543273; Tel: 34 963544419; E-mail: miguel.clemente@uv.es, eugenio.coronado@uv.es.

^b Centro de Ciências e Tecnologias Nucleares, DECN, Instituto Superior Técnico, Universidade de Lisboa, 2695-066 Bobadela LRS, Portugal.

Supporting Information

Table of contents

- 1. Experimental section**
 - Synthesis of 1
 - Synthesis of 2 and 3
 - Synthesis of Red_2, Red_3 and Reox_2
 - Syntheses of samples with exchange of solvents: 2·MeOH, 2·EtOH, 2·MeNO₂, 2·PhCN, 2·PhCN·MeCN and 2·PhCN·MeCN·PhCN.
 - Physical properties and crystallography
- 2. General Characterization of 1**
 - ¹H NMR of 1
 - IR spectroscopy of 1
 - ESI Mass of 1
 - Isotropic distribution of species of 1
 - Structure of 1
 - Simulated and experimental PXRD patterns of 1
- 3. Structural data for 2·MeCN, 3·MeCN, Red_2 and Red_3**
 - Pawley refinements
 - Crystallographic data
 - Short interchain contacts in 3
- 4. General characterization for solvent exchanged samples**
 - PXRD of solvated, desolvated and resolvated 2·MeCN
 - ¹H NMR of exchanged samples
 - TGA of exchanged samples
 - ¹H NMR, PXRD and TGA of reversibility experiments
 - PXRD of exchanged samples
 - Magnetic data for reversible experiments
 - Magnetic data of solvated, desolvated and desolvated 2·MeCN
- 5. General characterization of Red_2, Red_3 and Reox_2**
 - Cyclic Voltamperometry
 - IR Spectroscopy
 - XPS
 - ¹H NMR
 - PXRD of solvated and desolvated Red_2
 - PXRD of 2·MeCN, Red_2 and Reox_2
 - Structure of impurity of Reox_2
 - Mössbauer data for 2·MeCN
 - Magnetism of Red_3
 - EPR data of Red_3
- 6. References**

1. Experimental section

(C₁₆H₃₆N)₃[H₃V₁₀O₂₈]¹ and TRIS-bpp (See Scheme S1)² were synthesized according to the literature. All other materials and solvents were commercially available and used without further purification. Syntheses of **2**, **red_2** and **Red_3** were performed in a glove box.

i. Synthesis of **1**

Synthesis of (C₁₆H₃₆N)₂[V₆O₁₉(C₁₆H₁₅N₆O)₂]·(C₄H₉NO)₂ (**1**).

(C₁₆H₃₆N)₃[H₃V₁₀O₂₈] (1 g, 0.6 mmol) and TRIS-bpp (0.54 g, 1.5 mmol) were dissolved in 12 mL of dry dimethylacetamide (DMA) and heated to 80°C under an Ar atmosphere. After 48 hours a brownish solution was obtained and filtered. Red cubic shaped crystals (600 mg, 54%) were obtained after 5 days of slow evaporation of the solvent. ¹H NMR (CD₃CN, 300 MHz): 8.741 (d, J = 2.7 Hz, 4H, H_{Im1}), 8.11 (br, 4H, H_{Pyr}), 7.831 (d, J = 1.5 Hz, 4H, H_{Im2}), 6.59 (dd, J = 2.7, 0.9 Hz, 4H, H_{Im3}), 5.49 (s, 12H, H_{CH2}), 3.13 (m, 16H, H_{C1}), 1.62 (q, J = 7.8 Hz, 16H, H_{C2}), 1.36 (sx, J = 7.5 Hz, 16H, H_{C3}), 0.99 (t, J = 7.5 Hz, 24H, H_{C4}) (presence of 2 equiv. of DMA confirmed by peaks at 1.74, 2.85 and 2.99 ppm). IR (KBr pellet, cm⁻¹): 2959 (ν C-H, s), 2935 (ν C-H, s), 2874 (ν C-H, s), 1673 (m), 1627 (s), 1569 (m), 1549 (m), 1524 (m), 1484 (sh), 1460 (s), 1396 (ν C-H, s), 1362 (w), 1320 (w), 1284 (w), 1258 (w), 1207 (w), 1097 (ν C-O, s), 1057 (ν C-O, vs), 986 (w), 953 (ν V=O, vs), 882 (w), 812 (ν V-O-V, s), 800 (ν V-O-V, s), 767 (w), 719 (ν V-O-V, vs), 681 (w), 610 (w), 584 (m), 513 (w), 467 (w), 420 (m). Anal. Calcd (found) for (C₁₆H₃₆N)₂[V₆O₁₉(C₁₆H₁₅N₆O)₂]·(C₄H₉NO)₂: C, 45.91 (46.11); H, 6.42 (6.61); N, 11.90 (11.99) %.

ii. Synthesis of **2** and **3**

Synthesis of Fe[V₆O₁₉(C₁₆H₁₅N₆O)₂]·solv (**2**·DMF and **2**·MeCN).

A solution of **1** in dry dimethylformamide (DMF) (6 mL, 5 mM) was added to the bottom of a 16 mL diffusion tube. On top of this solution, a solution of Fe(ClO₄)₂·xH₂O in dry MeCN was added slowly (6 mL, 5 mM). After 2 weeks a crystalline material was found in the walls of the diffusion tube. It was collected and washed with MeCN several times. Samples were stored under fresh dry MeCN. IR (cm⁻¹): 3092 (w), 1675 (m), 1628 (m), 1573 (w), 1525 (m), 1498 (sh), 1458 (s), 1403 (ν C-H, s), 1318 (w), 1268 (w), 1207 (w), 1100 (ν C-O, s), 1046 (ν C-O, vs), 946 (ν V=O, vs), 865 (w), 789 (m), 707 (ν V-O-V, s), 577 (m), 511 (w), 456 (w), 420 (m). Anal. Calcd (found) for Fe[V₆O₁₉(C₁₆H₁₅N₆O)₂]·DMF·MeCN·5H₂O (**2**·DMF): C, 29.94 (29.85); N, 13.21 (13.31); H, 3.40 (3.34) (Filtered sample of the as-synthesized crystals). Anal. Calcd (found) for Fe[V₆O₁₉(C₁₆H₁₅N₆O)₂]·7H₂O (**2**·MeCN): C, 27.33 (27.34); N, 11.95 (11.95); H, 3.15 (3.00) (Filtered sample, stored in MeCN). Anal. Calcd (found) for Fe[V₆O₁₉(C₁₆H₁₅N₆O)₂]·5H₂O: C, 28.05 (28.18); N, 12.27 (12.15); H, 3.15 (2.94) (Sample heated to 400 K).

Synthesis of Zn[V₆O₁₉(C₁₆H₁₅N₆O)₂]·solv (**3**·DMF and **3**·MeCN).

Two different methods were employed in the synthesis of the zinc derivative. Method I was used to obtain single crystals and method II to obtain bulk material.

Method I. A solution of **1** in DMF (6 mL, 5 mM) was added to the bottom of a 16 mL diffusion tube in air. A mixture of 2 mL of MeCN and 2 mL of DMF was added on top of this solution as an interface between the two reactant solutions. A solution of Zn(ClO₄)₂ in MeCN (6 mL, 5 mM) was added slowly on top of this solution. After several weeks, very few single crystals of **3** were found in the walls of the diffusion tube, which were used to determine the single crystal structure without washing with MeCN (**3**·DMF sample). Anal. Calcd (found) for Zn[V₆O₁₉(C₁₆H₁₅N₆O)₂]·DMF·MeCN·6.5H₂O (**3**·DMF): C, 29.22 (29.21); N, 12.89 (12.90); H, 3.51 (3.43).

Method II. A solution of **1** in a 10:1 mixture of MeCN and DMF (6 mL, 5 mM) was added to the bottom of a 16 mL diffusion tube in a glove box. 2 mL of MeCN with one drop of DMF was added on top of this solution as an interface. Finally, a solution of Zn(ClO₄)₂ in MeCN (6 mL, 5 mM) was added slowly. After 3 days a crystalline powder material was found in the walls of the diffusion tube, it was collected and washed with acetonitrile several times (**3**·MeCN sample). IR (cm⁻¹): 3099(w), 1685 (m), 1630 (w), 1577 (w), 1528 (m), 1500 (sh), 1457 (s), 1403 (ν C-H, s), 1336 (w), 1268 (m), 1211 (w), 1096 (ν C-O, s), 1046 (ν C-O, vs), 946 (ν V=O, vs), 863 (w), 791 (m), 707 (ν V-O-V, s), 577 (m), 509 (w), 456 (w), 420 (m). Anal. Calcd (found) for Zn[V₆O₁₉(C₁₆H₁₅N₆O)₂]·6H₂O (**3**·MeCN): C, 27.50 (27.46); N, 12.02 (12.09); H, 3.03 (2.93).

iii. Synthesis of **Red_2**, **Red_3** and **Reox_2**

Synthesis of Fe[V₆O₁₉(C₁₆H₁₅N₆O)₂]·[Co(C₅H₅)₂]_{1.2}·8H₂O (**Red_2**) and Zn[V₆O₁₉(C₁₆H₁₅N₆O)₂]·[Co(C₅H₅)₂]_{1.2}·11H₂O (**Red_3**).

In a glovebox, bis(cyclopentadienyl)cobalt(II) (50 mg, 0.26 mmol) was dissolved in 10 mL of MeCN. To this solution, **2**·MeCN or **3**·MeCN (20 mg, 0.015 mmol) were added. The suspension

was slowly stirred for 5 hours. A rapid change in color during the first minutes was observed from orange to dark green. Dissolution of the crystals during this process was not observed. After this reaction time, supernatant was removed without leaving the crystals uncovered and the sample was washed with dry MeCN three times. IR (cm^{-1}): 3090 (w), 1652 (m), 1630 (w), 1567(w), 1524 (m), 1499 (sh), 1459 (s), 1404 (ν C-H, s), 1330 (w), 1267 (m), 1101 (ν C-O, s), 1045 (ν C-O, vs), 935 (ν V=O, vs), 863 (w), 796 (sh), 753 (ν V-O-V, s), 714 (s), 681 (s), 580 (s), 494 (w), 456 (w), 409 (m) (**Red_2**); 3080 (w), 1651 (m), 1630 (w), 1567(w), 1526 (m), 1500 (sh), 1456 (s), 1400 (ν C-H, s), 1333 (w), 1267 (m), 1103 (ν C-O, s), 1044 (ν C-O, vs), 974 (m), 930 (ν V=O, vs), 863 (w), 796 (sh), 754 (ν V-O-V, s), 678 (s), 582 (s), 494 (w), 456 (w), 405 (m) (**Red_3**). Anal. Calcd (found) for $\text{Fe}[\text{V}_6\text{O}_{19}(\text{C}_{16}\text{H}_{15}\text{N}_6\text{O})_2] \cdot [\text{Co}(\text{C}_5\text{H}_5)_2]_{1.3} \cdot 8\text{H}_2\text{O}$ (**Red_2**): C, 32.36 (32.27); N, 10.06 (9.86); H, 3.56 (3.50). Anal. Calcd (found) for $\text{Zn}[\text{V}_6\text{O}_{19}(\text{C}_{16}\text{H}_{15}\text{N}_6\text{O})_2] \cdot [\text{Co}(\text{C}_5\text{H}_5)_2]_{1.3} \cdot 11\text{H}_2\text{O}$ (**Red_3**): C, 31.18 (31.07); N, 9.90 (10.21); H, 3.50 (3.25).

Synthesis of $\text{Fe}[\text{V}_6\text{O}_{19}(\text{C}_{16}\text{H}_{15}\text{N}_6\text{O})_2][\text{Co}(\text{C}_5\text{H}_5)_2]_{0.5}[\text{Br}]_{0.5} \cdot 10\text{H}_2\text{O}$ (**Reox_2**).

Red_2 (20 mg) was suspended in MeCN. 30mg of TBABr₃ were then added to the suspension and slow stirring for 18 hours was employed. After this time, supernatant was removed without leaving the crystals uncovered and the sample was washed with dry MeCN several times. IR (cm^{-1}): 3096 (w), 1685 (w), 1628 (w), 1567(w), 1524 (m), 1499 (sh), 1459 (s), 1403 (ν C-H, s), 1322 (w), 1267 (m), 1208 (w), 1098 (ν C-O, m), 1047 (ν C-O, vs), 951 (ν V=O, vs), 863 (w), 792 (m), 710 (ν V-O-V, s), 577(m), 509 (w), 457 (w). Anal. Calcd (found) for $\text{Fe}[\text{V}_6\text{O}_{19}(\text{C}_{16}\text{H}_{15}\text{N}_6\text{O})_2] \cdot [\text{Co}(\text{C}_5\text{H}_5)_2]_{0.5}[\text{Br}_5]_{0.5} \cdot 10\text{H}_2\text{O}$ (**Reox_2**): C, 28.40 (28.42); N, 10.46 (10.62); H, 3.45 (3.49).

iv. Syntheses of samples with exchange of solvents: **2·MeOH**, **2·MeNO₂**, **2·EtOH**, **2·PhCN**, **2·PhCN·MeCN** and **2·PhCN·MeCN·PhCN**.

Most of the mother liquor (DMF/MeCN mixture) was removed leaving a small volume covering the crystals of **2·DMF** to avoid complete desolvation and loss of crystallinity. The exchanged solvent (MeOH, MeNO₂, EtOH or PhCN) was added covering the crystals for 3 days. During this time, several additions of clean solvent were performed without leaving the crystals uncovered. Finally, the exchanged material was stored in the same solvent. **2·PhCN·MeCN** was prepared in the same way starting from crystals of **2·PhCN**, which were soaked for 3 days in MeCN. **2·PhCN·MeCN·PhCN** was prepared in the same way soaking crystals of **2·PhCN·MeCN** for 3 days in PhCN. Anal. Calcd (found) for $\text{Fe}[\text{V}_6\text{O}_{19}(\text{C}_{16}\text{H}_{15}\text{N}_6\text{O})_2] \cdot 5.5\text{H}_2\text{O}$ (**2·MeOH**): C, 27.84 (27.84); N, 12.18 (12.34); H, 2.99 (3.01). Anal. Calcd (found) for $\text{Fe}[\text{V}_6\text{O}_{19}(\text{C}_{16}\text{H}_{15}\text{N}_6\text{O})_2] \cdot 3\text{H}_2\text{O}$ (**2·EtOH**): C, 28.42 (28.60); N, 12.43 (12.09); H, 2.83 (3.12). Anal. Calcd (found) for $\text{Fe}[\text{V}_6\text{O}_{19}(\text{C}_{16}\text{H}_{15}\text{N}_6\text{O})_2] \cdot 0.8\text{MeNO}_2 \cdot 4\text{H}_2\text{O}$ (**2·MeNO₂**): C, 27.69 (27.63); N, 12.11 (12.01); H, 3.05 (3.12). Anal. Calcd (found) for $\text{Fe}[\text{V}_6\text{O}_{19}(\text{C}_{16}\text{H}_{15}\text{N}_6\text{O})_2] \cdot 3\text{PhCN} \cdot 2\text{H}_2\text{O}$ (**2·PhCN**): C, 39.16 (39.03); N, 12.95 (13.19); H, 3.04 (3.24). Anal. Calcd (found) for $\text{Fe}[\text{V}_6\text{O}_{19}(\text{C}_{16}\text{H}_{15}\text{N}_6\text{O})_2] \cdot 6\text{H}_2\text{O}$ (**2·PhCN·MeCN**): C, 27.69 (27.58); N, 12.11(12.10); H, 3.05 (2.98). Anal. Calcd (found) for $\text{Fe}[\text{V}_6\text{O}_{19}(\text{C}_{16}\text{H}_{15}\text{N}_6\text{O})_2] \cdot 3\text{PhCN} \cdot 2\text{H}_2\text{O}$ (**2·PhCN·MeCN·PhCN**): C, 39.16 (39.23); N, 12.95 (13.12); H, 3.04 (3.15).

iv. Physical measurements and crystallography

IR spectra (cm^{-1}) were measured on an ATI Mattson Genesis Series FTIR instrument and a Nicolet Avatar 320 FTIR spectrometer. C, H and N elemental analyses were done using a CE Instruments EA 1110 CHNS Elemental analyser. The V:Fe, V:Zn, Co:Fe:V, Co:Zn:V and Co:Fe:V:Br ratios were measured using a Philips ESEM X230 scanning electron microscope equipped with an EDAX DX-4 microprobe. ¹H NMR spectra were acquired using a Bruker AVANCE DRX 300 spectrometer. A Q-TOF Premier mass spectrometer with an orthogonal Z-spray electrospray source (Waters, Manchester, UK) was used for electrospray ionization mass spectrometry (ESI-MS). The temperature of the source block was set to 100 1C and the desolvation temperature to 120 1C. A capillary voltage of 3.3 kV was used in the negative scan mode, and the cone voltage was set to 5 V to control the extent of fragmentation of the identified species. TOF mass spectra were acquired in the W-mode operating at a resolution of ca. 15 000 (fwhm). Mass calibration was performed using a solution of sodium iodide in isopropanol/water (50 : 50) from m/z 50 to 3000. Acetonitrile sample solutions were infused via syringe pump directly connected to the ESI source at a flow rate of 10 mL min⁻¹. The observed isotopic pattern of each compound perfectly matched the theoretical isotope pattern calculated from their

elemental composition using the MassLynx 4.1 program. TGA was performed in Mettler Toledo TGA/SDTA 851e Thermogravimetric and Differential Thermal Analyzer. XPS (K-ALPHA, Thermo Scientific) was used to analyze the surfaces of the samples. All spectra were collected using Al K α radiation (1486.6 eV), monochromatized by a twin crystal monochromator.

Single crystals of **1**, **3**·DMF and **Red_3** were mounted on glass fibres using a viscous hydrocarbon oil to coat the crystal and then were transferred directly to the cold nitrogen stream for data collection. All reflection data were collected at 120 K using a Supernova equipped with a graphite-monochromated Enhance (Mo) X-ray Source ($\lambda = 0.7107 \text{ \AA}$). The CrysAlisPro program, Oxford Diffraction Ltd., was used for unit cell determinations and data reduction. Empirical absorption correction was performed using spherical harmonics, implemented in the SCALE3 ABSPACK scaling algorithm. The structures were solved with the ShelXT structure solution program³ and refined with the SHELXL-2013 program,⁴ using Olex2.⁵ All non-hydrogen atoms were refined anisotropically except as noted and hydrogen atoms were placed in calculated positions and refined isotropically with a riding model. The structures of **3** and **Red_3** showed a weak diffraction due to the presence of disordered solvent molecules. Due to this, it was not possible to refine anisotropically O, C and N atoms and. In addition to this, high Rint, R1 and wR2 values were obtained. Initial refinements revealed the presence of a substantial volume of unresolvable solvent molecules in **3** (DMF) and **Red_3** (H₂O). It was removed from the electron density map using the OLEX solvent mask command. Two voids of 709.5 \AA^3 were found in the unit cell of **3** occupied by approximately 100 e⁻, giving a void volume of 22.3%. Two voids of 444.5 \AA^3 and two voids of 36.6 \AA^3 were found in the unit cell of **Red_3** occupied by approximately 46 e⁻ and 8e⁻, respectively, giving a void volume of 15.2%. Crystallographic data are summarized in Table S1. Crystallographic data for the structures were deposited in the Cambridge Crystallographic Data Centre, deposition numbers CCDC 2213981-4. These data can be obtained free of charge from The Cambridge Crystallographic Data Centre via www.ccdc.cam.ac.uk/data_request/cif.

Polycrystalline samples were filled into 0.7 and 1 mm borosilicate capillaries prior to being mounted and aligned on an Empyrean PANalytical powder diffractometer, using Cu K α radiation ($\lambda = 1.54056 \text{ \AA}$). For each compound, three repeated measurements were collected at room temperature ($2\theta = 2\text{--}40^\circ$) and merged in a single diffractogram. Pawley refinements⁶ were performed using the TOPAS computer program⁷ and revealed an excellent fit to a one-phase model for compounds **2** ($R_{wp} = 0.0201$; GOF = 7.447, Fig. S7a), **3** ($R_{wp} = 0.0151$; GOF = 2.2432, Fig. S7b), **Red_2** ($R_{wp} = 0.0113$; GOF = 1.480, Fig. S7c) and **Red_3** ($R_{wp} = 0.0124$; GOF = 1.620, Fig. S7d). The unit cell parameters for each compound are shown in Table S2. In the Zn derivatives, the unit cell obtained from the Pawley refinement is consistent with those obtained by single crystal diffraction (see Table S1).

The electrochemical experiments were performed using an Autolab electrochemical workstation (Autolab-128N potentiostat/galvanostat) connected to a personal computer that uses Nova 2.1 electrochemical software. The freshly filtered polycrystalline samples (2 mg) were mixed in 2 mL of Nafion 5% and ethanol (1:1) and deposited on a 3 mm diameter glassy carbon disc working electrode (which was polished sequentially with 0.3, 0.1 and 0.05 μm alumina powders and washed with deionised water before each experiment). A typical three-electrode experimental cell equipped with a platinum wire as the counter electrode, and a silver wire as the pseudoreference electrode was used for the electrochemical characterization of the working electrodes. All measurements were carried out with magnetic agitation and nitrogen bubbling. The electrochemical properties were studied measuring the CV at different scan rates in 0.1 M TBABF₄/CH₃CN solution. Ferrocene was added as an internal standard upon completion of each experiment. All potentials are reported in V versus Ag/AgCl

Magnetic measurements were performed with a Quantum Design MPMS-XL-5 SQUID magnetometer with an applied magnetic field of 0.1 T. Solvated polycrystalline samples were deposited in the bottom of a glass tube and covered with the mother liquor. This tube was used as the sample holder. Photomagnetic measurements were performed irradiating with a 30993 cylindrical Helium-Neon Laser system from Research Electro-Optics (red light, $\lambda = 633 \text{ nm}$, optical power 12 mW cm^{-2}) coupled via an optical fiber to the cavity of the SQUID magnetometer. It was verified that irradiation resulted in no significant change in magnetic response due to heating of the sample. The photomagnetic samples consisted of a thin layer of compound whose weight was corrected by comparison of a thermal spin crossover curve with that of a more accurately weighted sample of the same compound. Solvated samples were protected with a grease immediately after being extracted from the mother liquor. EPR measurements were recorded in a Bruker ELEXYS E580 spectrometer under X-band irradiation ($\sim 9.4 \text{ GHz}$) in

samples protected with the mother liquor and prepared and sealed in the glove box. Mössbauer spectra of 2 sample were collected between 295 and 4 K in transmission mode using a conventional constant-acceleration spectrometer and a 25 mCi ^{57}Co source in a Rh matrix. The velocity scale was calibrated using α -Fe foil. Isomer shifts, IS, are given relative to this standard at room temperature. The absorbers were obtained by gently packing the sample into a perspex holder. Absorber thickness was calculated on the basis of the corresponding electronic mass-absorption coefficients for the 14.4 keV radiation, according to Long *et al.* (1983).⁸ Low-temperature measurements were performed in a bath cryostat with the sample immersed in liquid He at 4 K, or in He exchange gas above 4 K. The spectra were fitted to Lorentzian lines using a non-linear least-squares method.⁹ Mössbauer spectra of the solvated samples could not be measured because the sample environment in the spectrophotometer between 273 and 200 K is under vacuum. This makes impossible measurements in contact with the mother liquid as those required for the solvated samples.

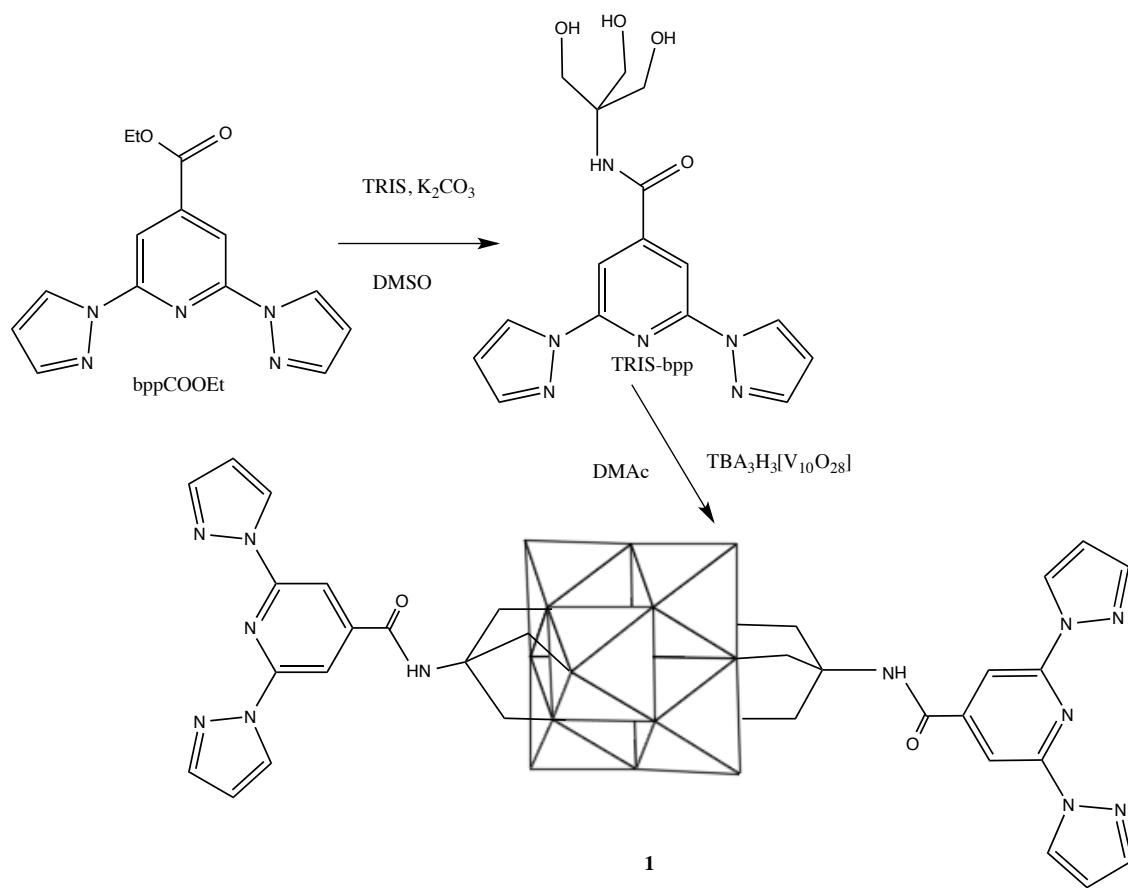
2. General Characterization of 1

1-bpp-functionalized Lindqvist POM (**1**) was synthesized following adapted literature procedures (see Scheme 1).^{2,10} The starting material for the preparation of the functionalized POM was a tris-(hydroxymethyl)-functionalized 1-bpp (TRIS-bpp), which was obtained from 1-bpp-4'-carboxyethyl ester.² The functionalization of the POM was performed by reaction of TRIS-bpp and the polyoxovanadate precursor, TBA₃H₃[V₁₀O₂₈] (TBA = tetrabutylammonium), in dry dimethylacetamide (DMA). Single crystals were obtained by slow evaporation of the DMA solution of the compound. ¹H NMR spectra confirm the purity of **1** and the grafting of 1-bpp to the POM in **1** (see **Fig. S1**). As observed previously in terpyridine-functionalized Lindqvist POM,¹⁰ the electronic influence of the cluster (diamagnetic V^V) induces changes in the chemical shifts of the methylene protons of the ligand but not in those of the aromatic ones. Further characterization of **1** has been performed by elemental analysis, IR spectroscopy (**Fig. S2**), and electrospray ionization mass spectrometry (ESI-MS) (**Figs. S3 and S4**). Thus, the IR bands at 953 cm⁻¹ (ν V=O), 812, 800 and 719 cm⁻¹ (ν V-O-V), correspond to the Lindqvist structure,¹¹ while the bands at 1673 cm⁻¹ (ν C=O), 1097, and 1057 cm⁻¹ (ν C-O) confirm the grafting of TRIS-bpp onto the POM (**Fig. S2**). On the other hand, ESI-MS is consistent with the bifunctionalization of the POM. **Fig. S3** shows the ESI-MS (negative mode) analysis of a solution of **1** in acetonitrile. The two most intense peaks appear at m/z values of 611.9, and 1224.9, which correspond respectively to the [V₆O₁₉(C₁₆H₁₅N₆O)₂]²⁻ ([**1**]²⁻) and H[V₆O₁₉(C₁₆H₁₅N₆O)₂]⁻ (H⁺ + [**1**]²⁻) species. As these peaks arise from species in which the POM remains intact, we can conclude that the structure of the polyanion is preserved in solution. The charge of the species present in the spectrum has been characterized by single ion recording (SIR) at the highest resolution of the spectrometer with monoisotopic peaks separated by 1/z. **Fig. S4**, shows the isotopic distributions of the most intense peaks. The simulated profile does not fit exactly with the experimental one. This could be due to the presence of reduced vanadium centers (V(IV)) formed as a consequence of the high voltages utilized in the mass spectrometry ion-transfer process. Indeed, the presence of molybdenum and tungsten in reduced oxidation states in ESI-MS experiments of polyoxomolybdates and polyoxotungstates has been reported.¹² Furthermore, a similar effect seems to be observed in the ESI-MS spectrum of the same hexavanadate functionalized with terpyridine.¹⁰

Structure of (C₁₆H₃₆N)₂[V₆O₁₉(C₁₆H₁₅N₆O)₂]⁻·(C₄H₉NO)₂ (1**)**

1 crystallizes in the monoclinic space group *P*2₁/*c*. The asymmetric unit is composed by half crystallographically independent anion, one TBA⁺ cation and one DMA solvent molecule. The crystallographically independent anion contains an inversion centre placed in the central O atom, O7. It presents the common Lindqvist hexavanadate structure, in which the six V atoms from six octahedral edge-sharing VO₆ form an octahedron. The two trisalkoxy ligands occupy opposite faces of that octahedron (**Fig. 2**). The presence of the trisalkoxy ligands deforms the regular hexavanadate core as observed in similar compounds. Thus, **1** possesses six doubly bridging oxo groups and six doubly bridging alkoxy groups with average V-O distances of 1.827 (2) and 2.017(2) Å, respectively.¹⁰ The crystallographically independent POM is surrounded by TBA⁺ cations and solvent molecules (**Fig. S5**). Hydrogen bonds are observed between the two NH groups of the POMs and carbonyl group from DMA molecules. Furthermore, the POM presents π-π stacking interactions with the DMA molecule and numerous short contacts between the oxo group and the CH groups from TBA⁺ cations. In contrast to the terpyridine-hexavanadate derivative, clear π-π stacking interactions are not observed between 1-bpp units of neighbouring functionalized-POM. Thus, the pyrazole units from neighbouring functionalized POM present shortest contacts of 3.327 Å and are almost perpendicular (angle between the pyrazole rings close to 80.4°).

The phase purity of the bulk material was evaluated by PXRD. The experimental PXRD pattern at room temperature matches well with that of the calculated one from the single crystal data at 120 K confirming the purity of the compound (**Fig. S6**).



Scheme S1. Synthesis of TRIS-bpp and 1.

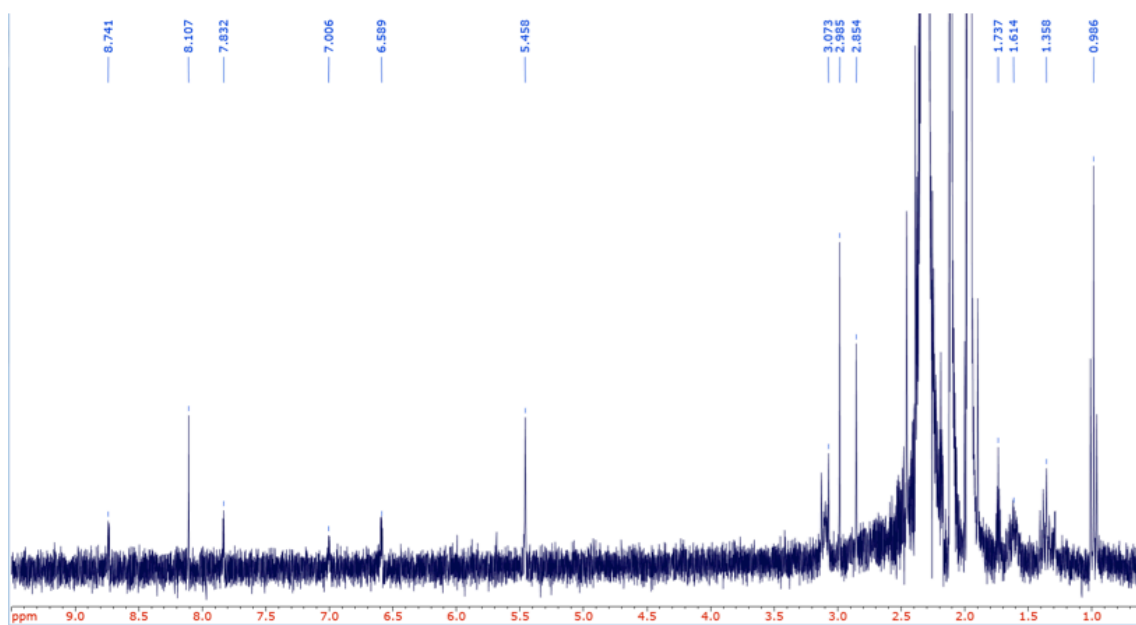


Fig. S1 ¹H NMR spectra of 1.

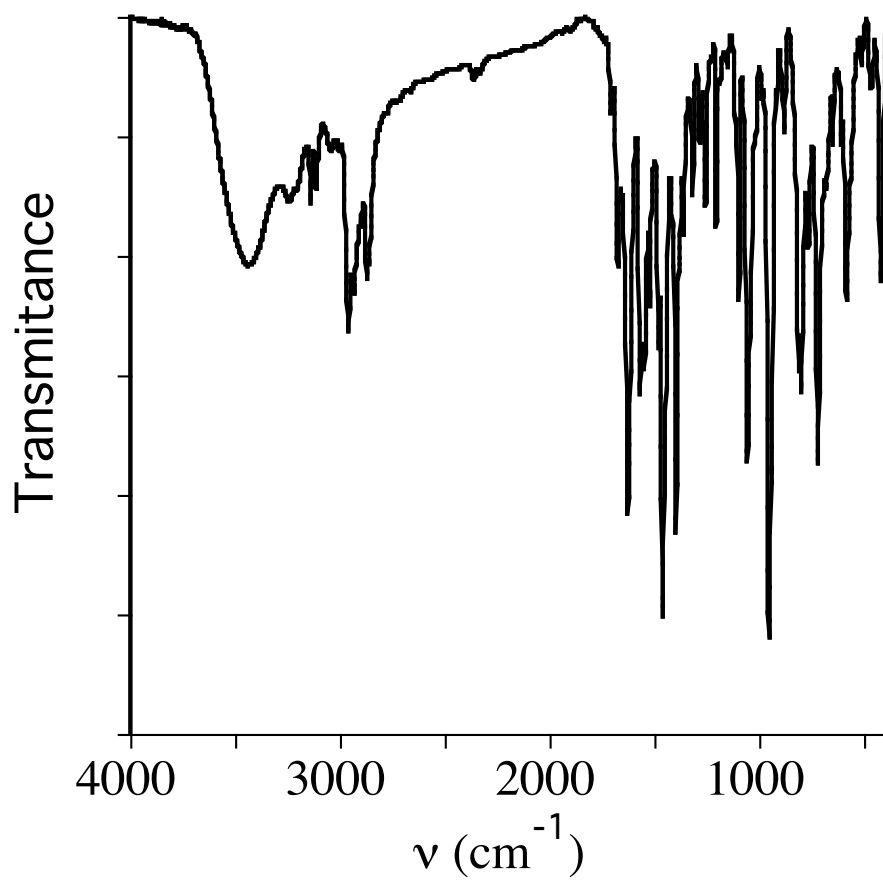


Fig. S2 IR spectrum of 1.

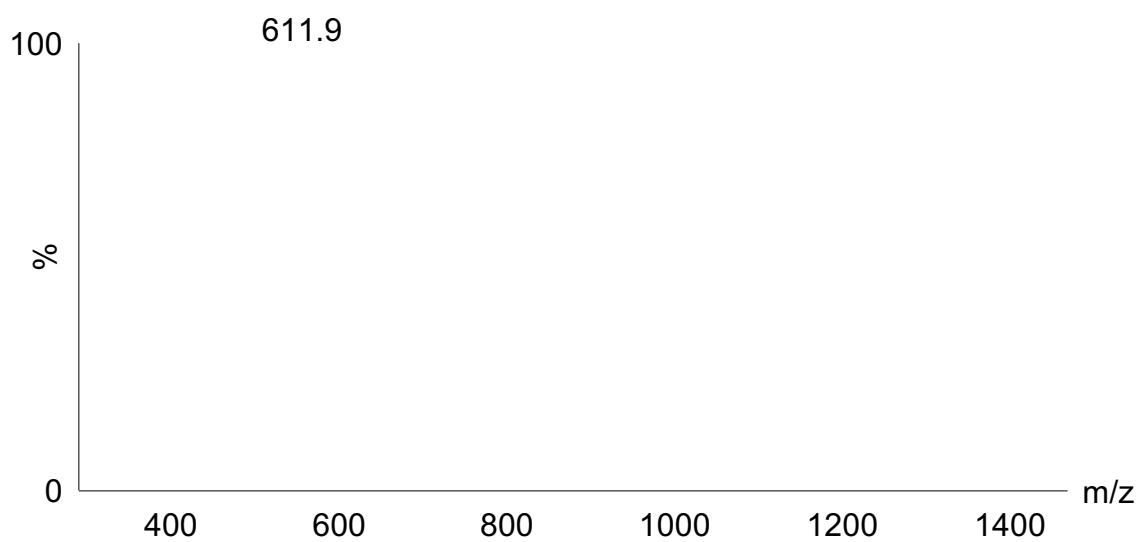


Fig. S3 ESI mass spectrum of acetonitrile solutions of compound **1** recorded at $U_c = 5$ V.

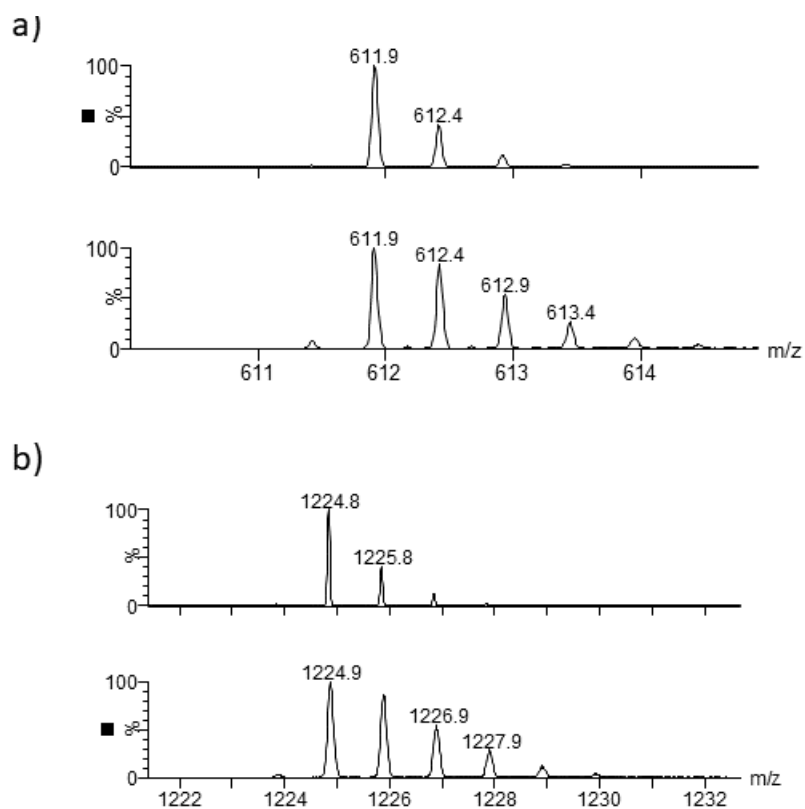


Fig. S4 Simulated (a) and experimental (b) isotopic distribution for the identified species, $[1]^{2-}$ (top) and $[1 + H]^{-}$ (bottom).

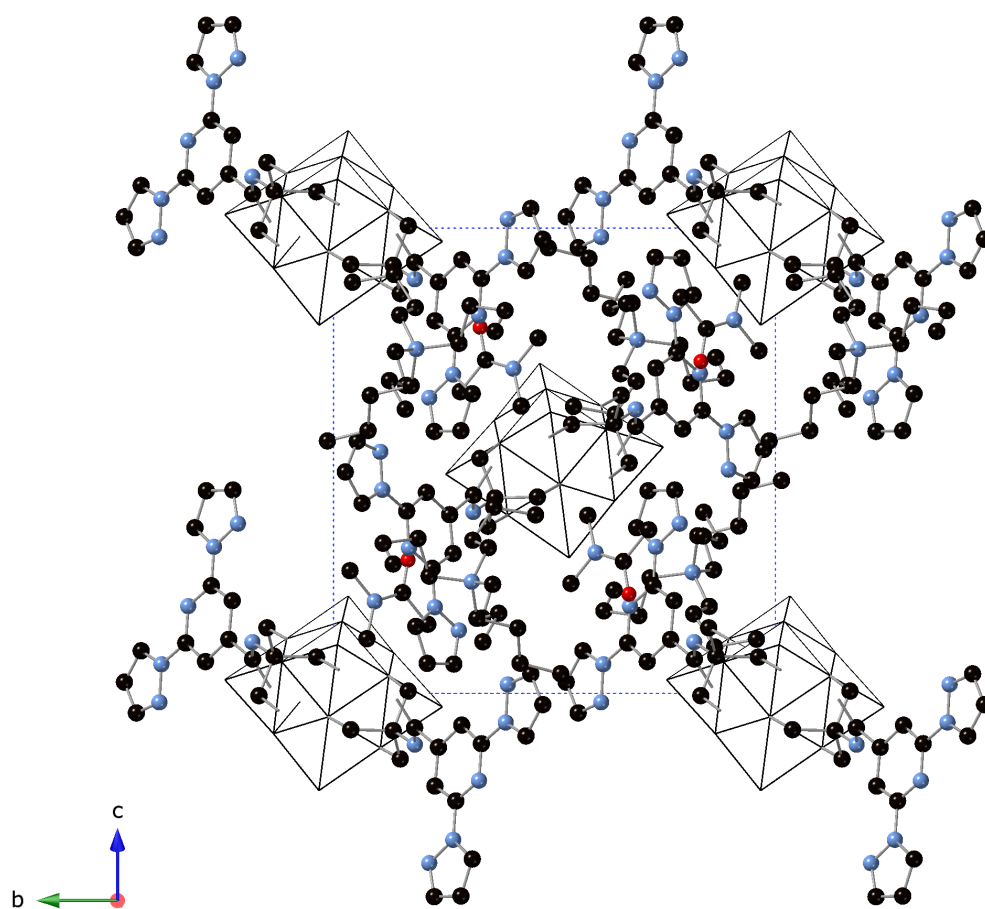


Fig. S5 Projection of the structure of **1** in the *bc* plane (V (white), C (black), N (blue), O (red)). Hydrogen atoms have been omitted for clarity.

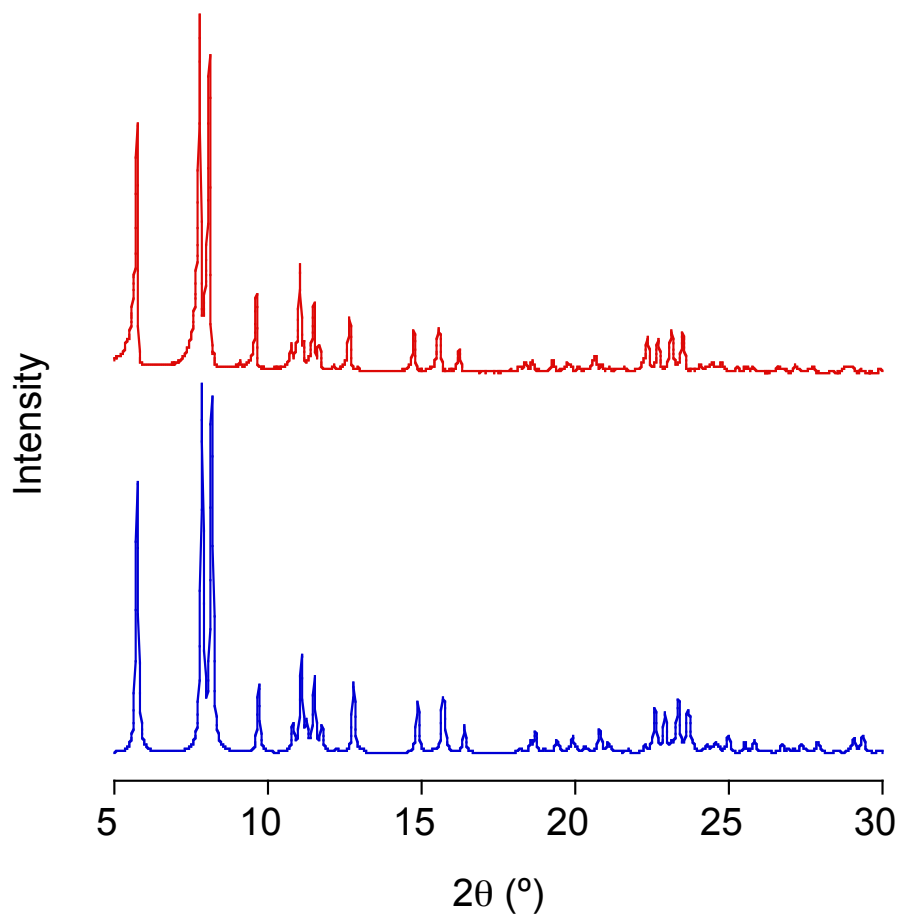


Fig. S6 Experimental (top) and simulated (bottom) X-ray powder diffraction patterns of **1**.

3. Structural data for 2·MeCN, 3·MeCN, Red 2 and Red 3

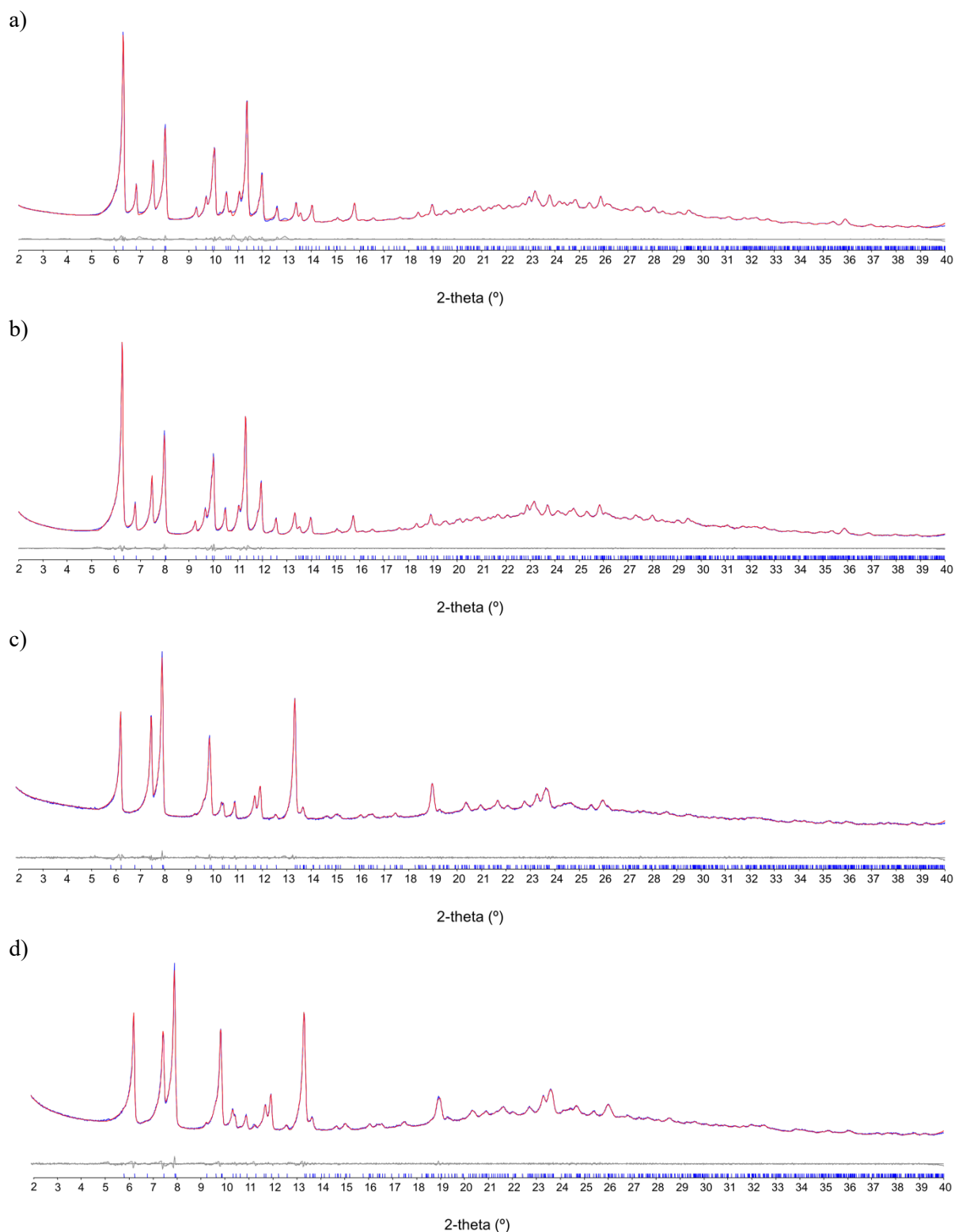


Figure S7. Observed (blue) and calculated (red) profiles and difference plot $[(I_{\text{obs}} - I_{\text{calcd}})]$ (grey) of the Pawley refinements of compounds 2·MeCN (a), 3·MeCN (b), Red 2 (c) and Red 3 (d). (2θ range 2–40 °; $\lambda = 1.54056 \text{ \AA}$).

Table S1. Crystallographic data for **1**, **3** and **Red_3**.[‡]

Compound	1	3	Red_3
Empirical formula	C ₇₂ H ₁₂₀ N ₁₆ O ₂₃ V ₆	C _{39.25} H _{45.25} N _{14.75} O _{22.75} V ₆ Zn	C ₄₂ H ₄₇ CoN ₁₂ O ₂₅ V ₆ Zn
Formula weight	1883.47	1458.66	1549.85
Temperature/K	120.2	120.2	293(2)
Crystal system	monoclinic	monoclinic	monoclinic
Space group	P2 ₁ /c	P2 ₁ /c	P2 ₁ /c
a/Å	17.1948(3)	13.2016(16)	13.0369(18)
b/Å	15.4967(2)	27.457(4)	27.261(3)
c/Å	18.2880(4)	18.236(2)	18.467(3)
α/°	90	90	90
β/°	116.713(3)	105.503(13)	105.569(15)
γ/°	90	90	90
Volume/Å ³	4352.96(17)	6369.8(15)	6322.5(16)
Z	2	4	4
ρ _{calc} /g/cm ³	1.437	1.521	1.628
μ/mm ⁻¹	0.697	1.292	1.558
F(000)	1972.0	2936.0	3112.0
Crystal size/mm ³	0.20 × 0.15 × 0.07	0.18 × 0.13 × 0.10	0.06 × 0.02 × 0.02
Radiation	MoKα (λ = 0.71073)	MoKα (λ = 0.71073)	MoKα (λ = 0.71073)
2θ range for data collection/°	6.62 to 55.038	6.474 to 41.628	6.45 to 34.51
Index ranges	-22 ≤ h ≤ 22, -20 ≤ k ≤ 20, -23 ≤ l ≤ 23	-13 ≤ h ≤ 13, -27 ≤ k ≤ 27, -18 ≤ l ≤ 18	-10 ≤ h ≤ 10, -22 ≤ k ≤ 22, -15 ≤ l ≤ 15
Reflections collected	114963	1146	41118
Independent reflections	9981 [R _{int} = 0.0848, R _{sigma} = 0.0420]	6645 [R _{int} = 0.3828, R _{sigma} = 0.2483]	3821 [R _{int} = 0.3572, R _{sigma} = 0.1714]
Data/restraints/parameters	9981/0/529	6645/0/377	3821/30/347
Goodness-of-fit on F ²	1.049	0.993	1.098
Final R indexes [I >= 2σ (I)]	R ₁ = 0.0492, wR ₂ = 0.1241	R ₁ = 0.1233, wR ₂ = 0.2771	R ₁ = 0.1281, wR ₂ = 0.3164
Final R indexes [all data]	R ₁ = 0.0722, wR ₂ = 0.1391	R ₁ = 0.2161, wR ₂ = 0.3308	R ₁ = 0.1950, wR ₂ = 0.3634
Largest diff. peak/hole / e Å ⁻³	0.59/-0.55	0.87/-0.78	1.83/-1.04

^[a]R₁(F) = Σ||F_o| - |F_c||/Σ|F_o|; ^[b]wR₂(F²) = [Σw(F_o² - F_c²)²/ΣwF_o⁴]^{1/2}; ^[c]S(F²) = [Σw(F_o² - F_c²)²/Σn + r - p]^{1/2}

Table S2. Unit cell parameters obtained from Pawley refinements for compounds **2·MeCN**, **Red_2**, **3·MeCN** and **Red_3**.

	a (Å)	b (Å)	c (Å)	α (°)	β (°)	γ (°)
2·MeCN	13.3974(9)	28.090(19)	18.2329(11)	90	104.910(4)	90
Red_2	13.2843(9)	27.9038(19)	18.3913(12)	90	105.135(5)	90
3·MeCN	13.3992(6)	28.085(13)	18.2259(7)	90	104.712(2)	90
Red_3	13.3114(12)	27.872(3)	18.3681(18)	90	104.804(6)	90
Data from single crystal:						
3·DMF	13.2014(14)	27.454(4)	18.232(2)	90	105.500(12)	90
Red_3	13.0362(19)	27.263(3)	18.471(3)	90	105.594(16)	90

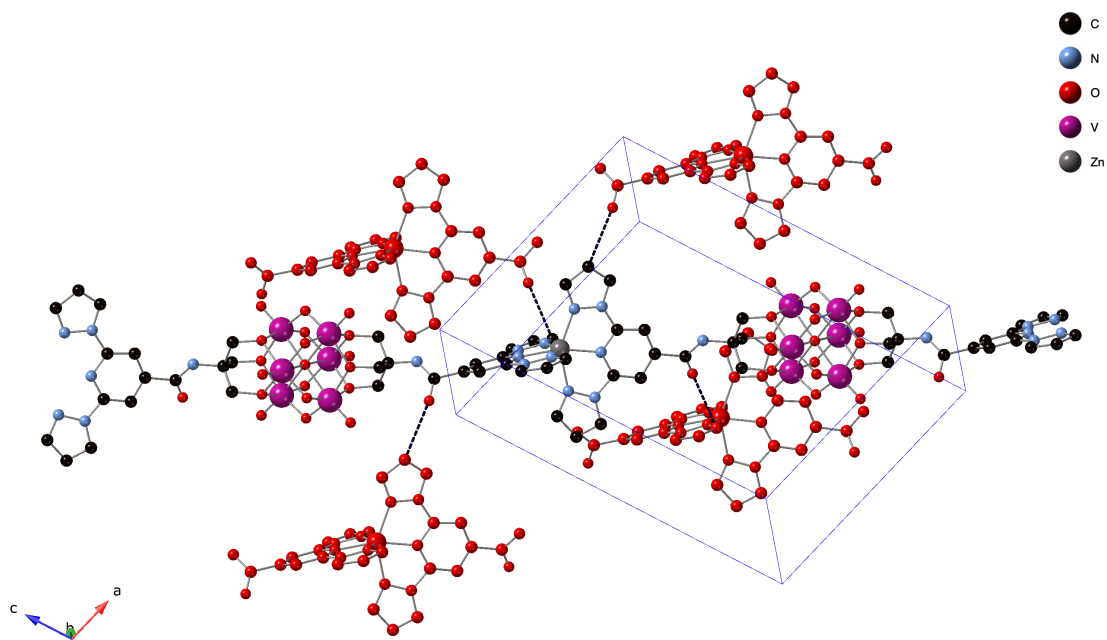


Figure S8. Short interchain contacts (blue dashed line) between $[\text{Zn}(\text{1-bpp})_2]^{2+}$ complexes. $[\text{Zn}(\text{1-bpp})_2]^{2+}$ complexes from neighboring chains are colored in red.

4. General characterization for solvent exchanged samples

PXRD pattern of a filtered sample of **2·MeCN** presents fewer and broader peaks than that of the solvated sample (see **Fig. S9**). These changes indicate a loss of crystallinity and a different packing of the $M[V_6O_{19}(C_{16}H_{15}N_6O)_2]$ chains upon desolvation. The shift of the most intense peak at lower theta values ($2\theta = 6.3^\circ$ in contact with the mother liquor to $2\theta = 6.9^\circ$ in the filtered sample), suggests that the space between chains is being reduced. Indeed, simulated PXRD from the single crystal structure of **3** reducing *b* parameter, which is related to the distance between the double layers, by 2 Å (from 27.4573 to 25.4573 Å) leads to similar features in the simulated PXRD pattern (see **Fig. S10**).

Whereas 1H NMR of **2·DMF** and **3·DMF** confirms the presence of DMF and MeCN found in the structure of **3·DMF** (see below and **Fig. S11** in the ESI), the samples with exchanged solvents present a variety of behaviors. In all of them, the intensity of the signals from DMF molecules is completely vanished (**2·MeCN** and **2·EtOH**) or reduced (**2·MeOH**, **2·MeNO₂** and **2·PhCN**) with respect to that of **2·DMF** or **3·DMF**. On the other hand, the signals from MeCN molecules observed in **2·DMF** completely disappear in **2·MeOH**, **2·EtOH**, **2·MeNO₂** and **2·PhCN**. The 1H NMR signals of the exchanged solvent are observed in **2·MeCN**, **3·MeCN**, **2·MeNO₂** and **2·PhCN** but not in the samples exchanged with alcohol solvents (**2·MeOH** and **2·EtOH**). Elemental analyses of the filtered samples, which showed a higher degree of desolvation because they were stored in air for longer times, are consistent with the presence of solvent molecules in the structure of the exchanged samples with less volatile solvents (**2·MeNO₂**, **2·PhCN**, **2·DMF** and **3·DMF**) and only water molecules in **2·MeCN**, **2·MeOH**, **2·EtOH** and **3·MeCN** (see experimental section in the ESI†). This is consistent with thermogravimetric (TG) analyses, which show weight losses below 100 °C and a plateau at higher temperatures for these last samples. In contrast, **2·PhCN** and **2·DMF** show gradual weight losses up to higher temperatures in the same range of those of decomposition of 1-bpp ligand around 180 °C (see **Fig. S12** in the ESI†). These results indicate that the organic solvent molecules found in the structure of **3·DMF** (DMF and MeCN) can be easily replaced by other solvents or water molecules. To test the reversibility of the process, we performed additional solvent exchanges in the sample with the bulkiest solvent (**2·PhCN**), which was subsequently soaked for 3 days in MeCN (sample **2·PhCN·MeCN**). Finally, **2·PhCN·MeCN** was successively soaked in PhCN for other 3 days (**2·PhCN·MeCN·PhCN**). 1H NMR and elemental analysis of these samples confirm replacement of PhCN by MeCN in **2·PhCN·MeCN**, which is successively replaced by PhCN in **2·PhCN·MeCN·PhCN** (see experimental section and **Fig. S13** in the ESI†). PXRD and magnetic data of these two samples are very similar to those of **2·MeCN** and **2·PhCN**, obtained from **2·DMF** (see **Fig. S13** in the ESI† and below). This confirms that the exchange of solvents is reversible.

PXRD patterns of these samples show differences in the relative intensity of the peaks due to the different pore filling. The PXRD pattern of **2·MeOH** displays broader peaks at similar positions as those of the filtered sample of **2·MeCN** (see above). This could suggest a collapse of the structure in this exchanged sample.

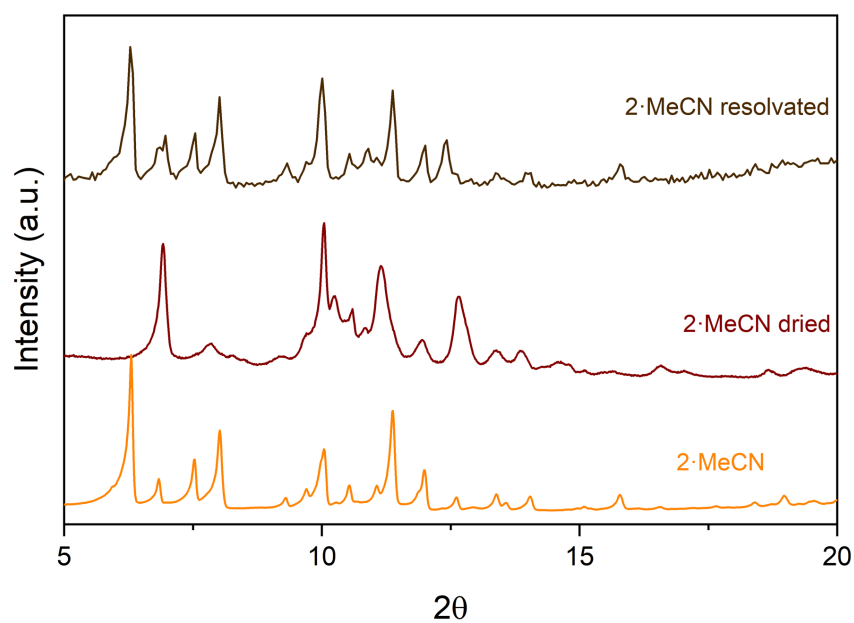


Fig. S9 PXR D patterns of **2·MeCN** in contact with the mother liquor (orange line), filtered sample of **2·MeCN** (brown line) and resolved **2·MeCN** in contact with the mother liquor (green line).

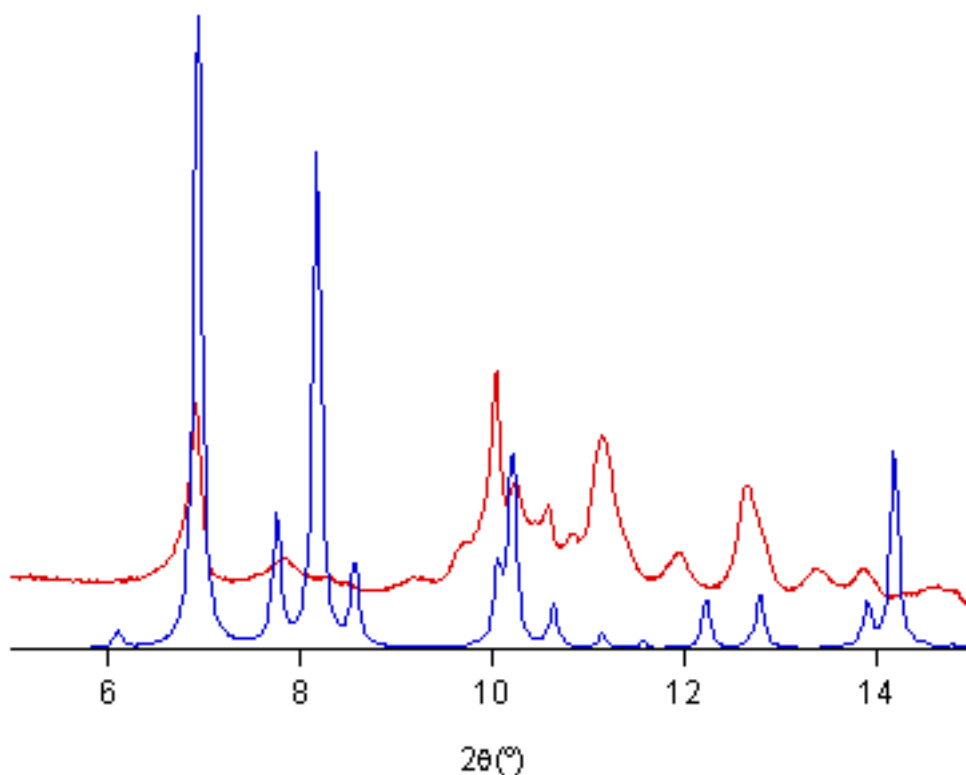


Fig. S10 Simulated PXR D pattern from the single crystal structure of **3·DMF** reducing by 2 \AA b parameter (blue line) and experimental PXR D pattern of a filtered sample of **2·MeCN** (red line).

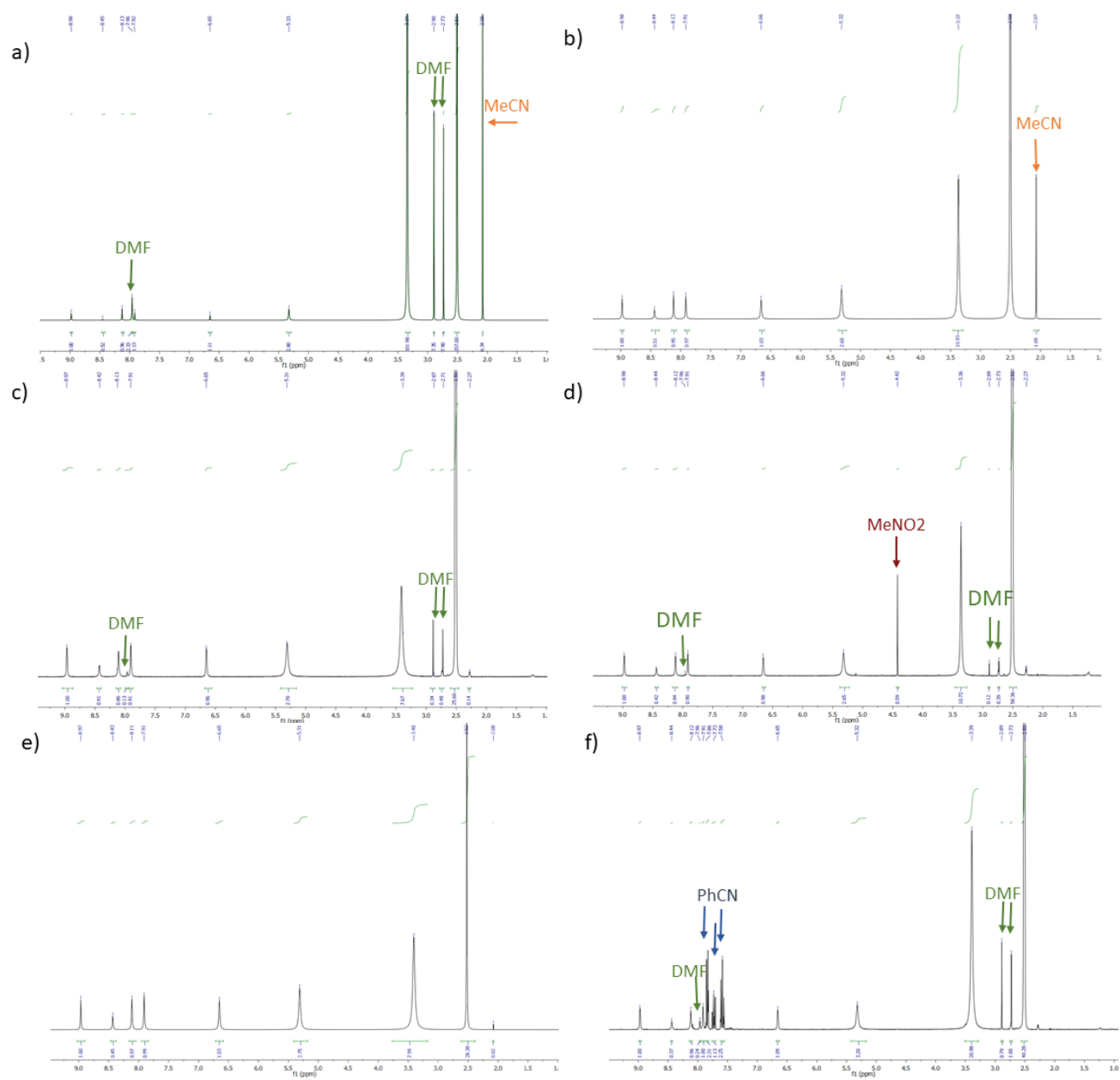


Fig. S11 ^1H NMR spectra of freshly filtered crystals of **2**·DMF (a), **2**·MeCN (b), **2**MeOH (c), **2**MeNO₂ (d), **2**·EtOH (e), **2**·PhCN (f).

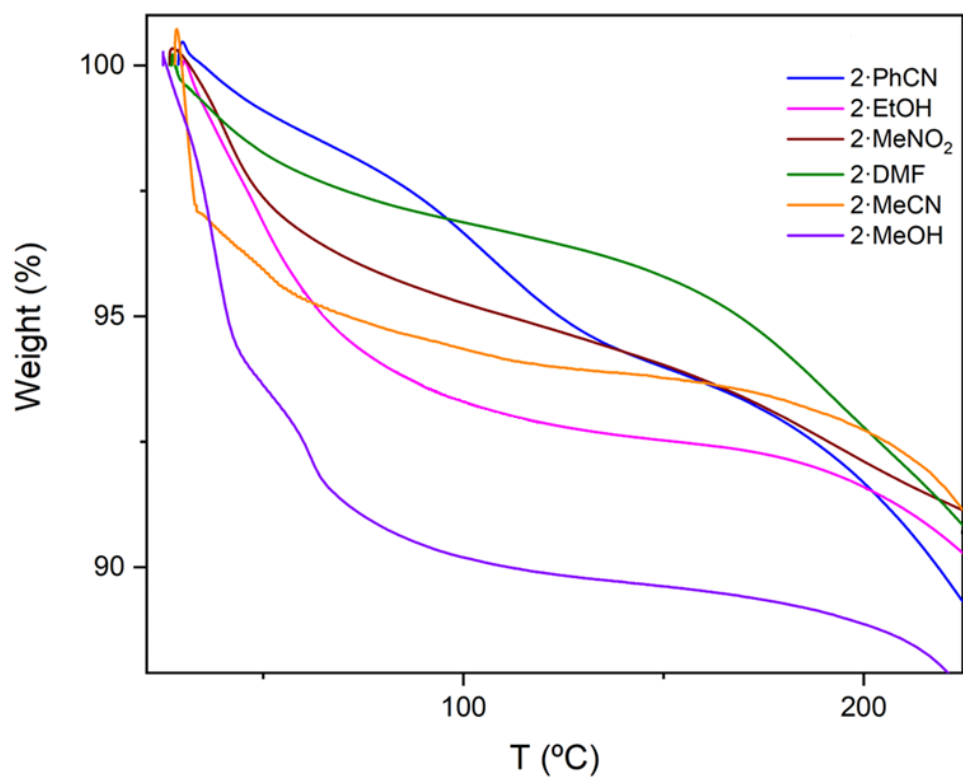
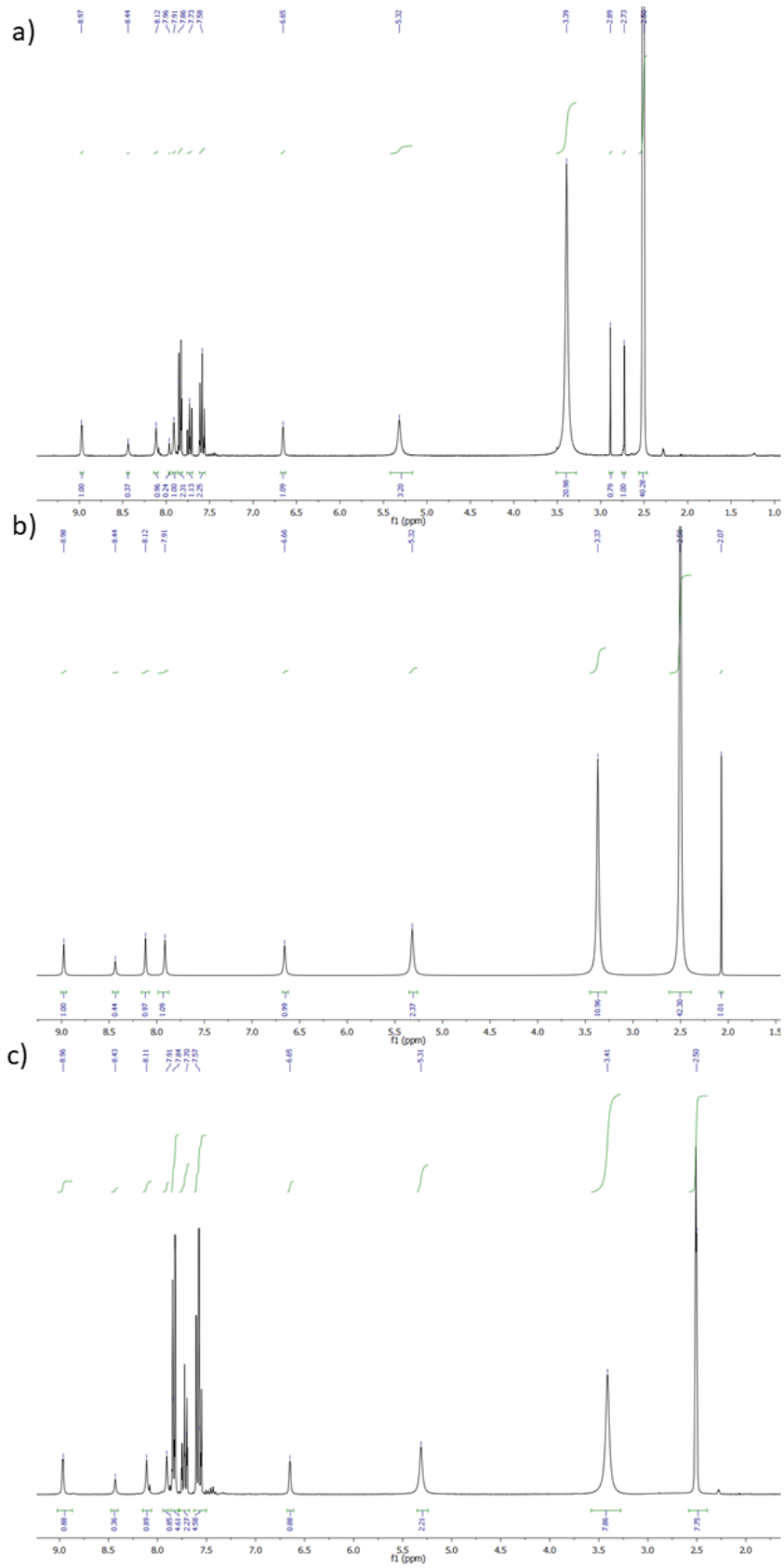
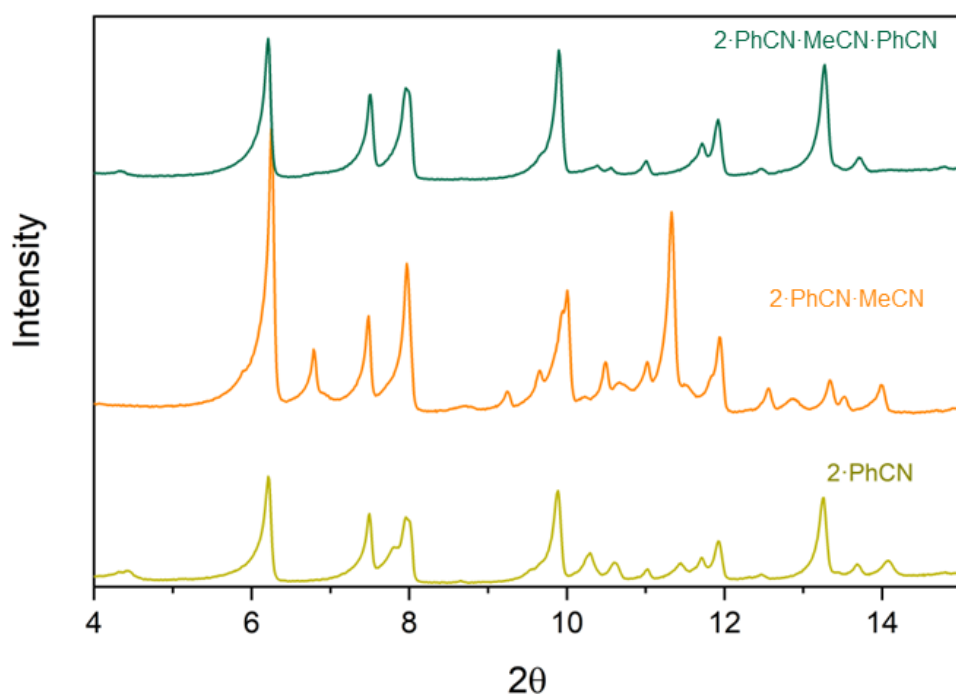


Fig. S12 Thermogravimetric analysis of **2·DMF**, **2·MeCN**, **2MeOH**, **2MeNO₂**, **2·EtOH** and **2·PhCN**.



d)



e)

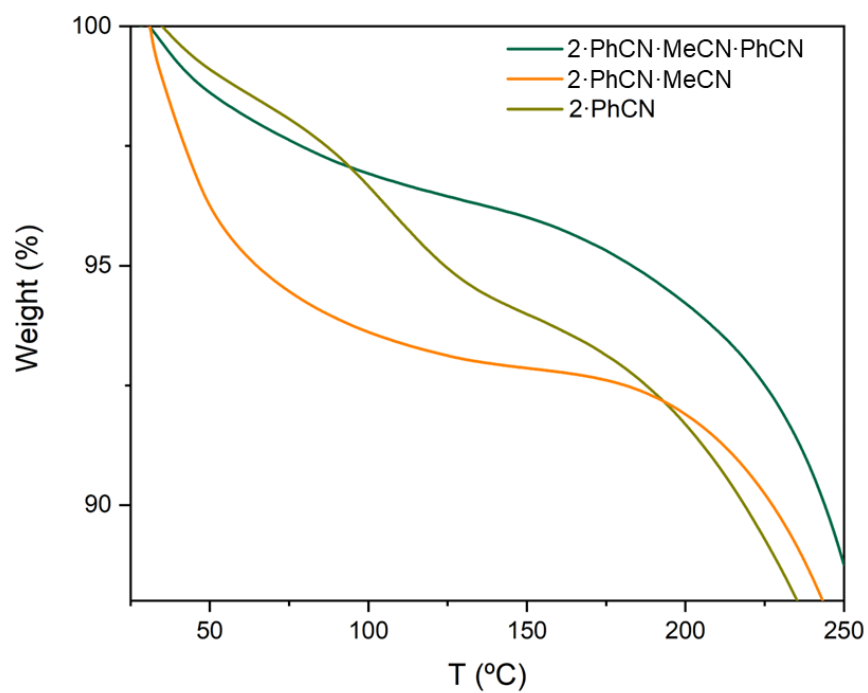


Fig. S13. ^1H NMR of freshly filtered crystals of **2·PhCN** (a), **2·PhCN·MeCN** (b) and **2·PhCN·MeCN·PhCN** (c). PXRD of the same samples measured in contact with the mother liquor (d), Thermogravimetric analysis of the same samples (e).

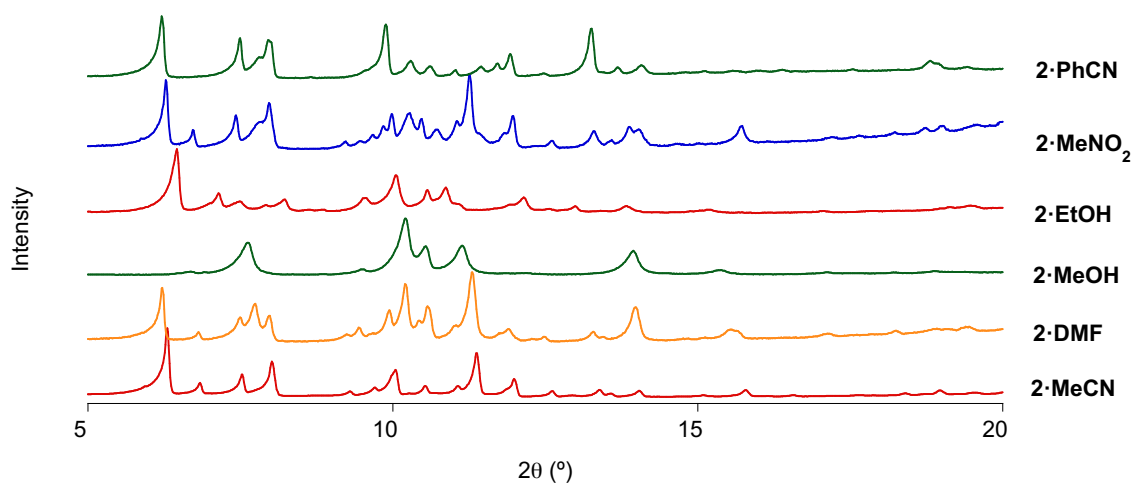


Fig. S14 PXR D patterns of **2·DMF**, **2·MeCN**, **2·MeOH**, **2·MeNO₂**, **2·EtOH** and **2·PhCN**.

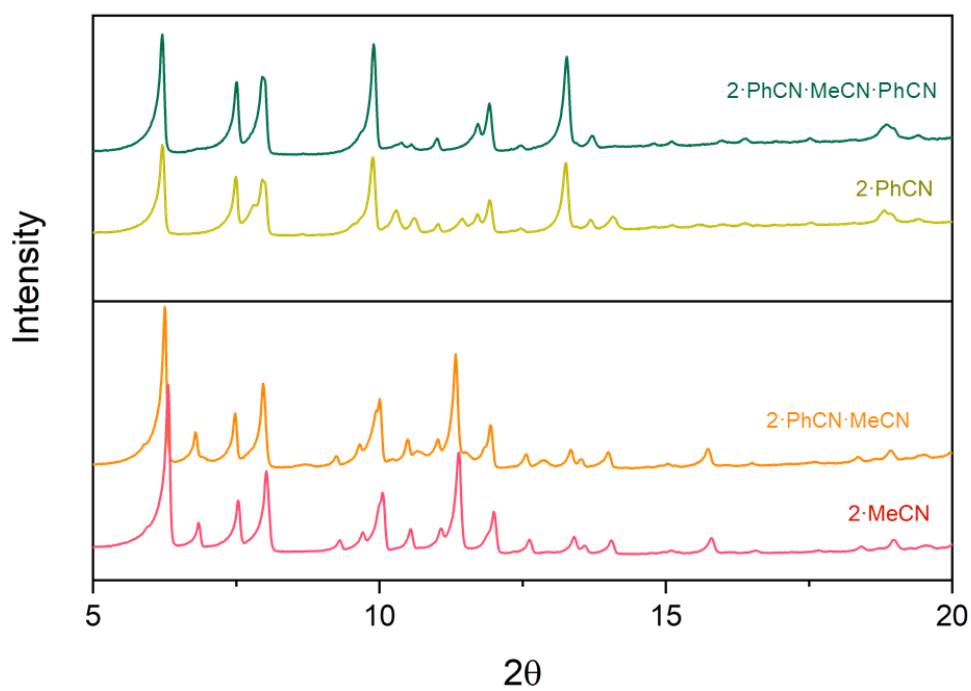


Fig. S15 PXR D patterns comparing structural similarities between **2·MeCN** and **2·PhCN·MeCN** (bottom) and between **2·PhCN** and **2·PhCN·MeCN·PhCN** (top).

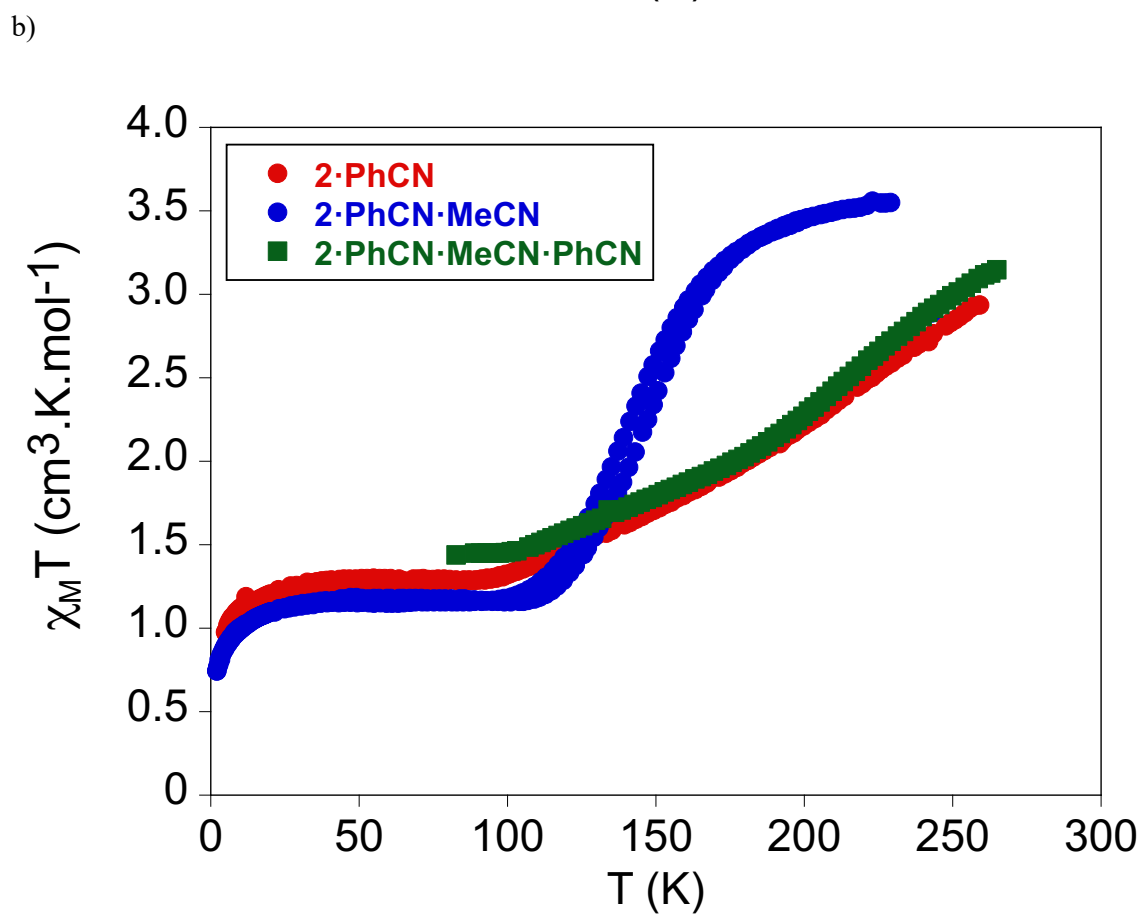
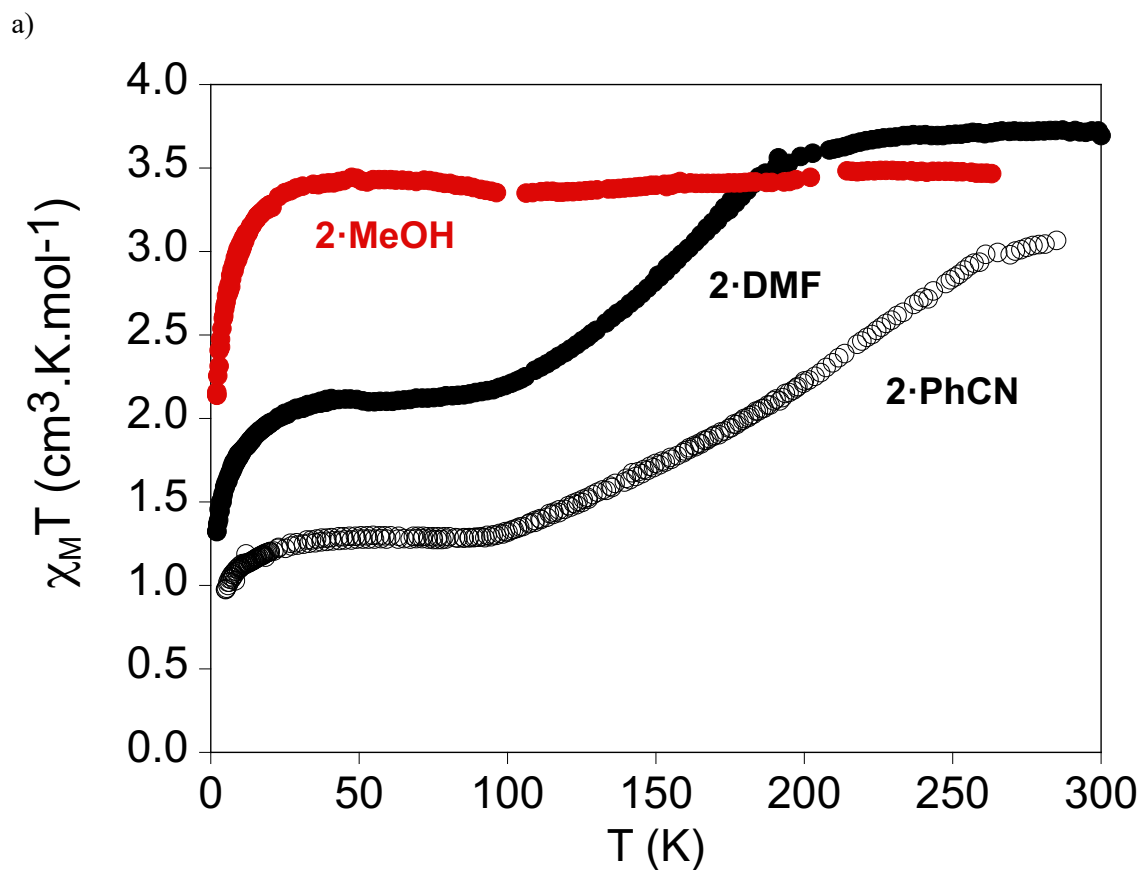


Fig. S16 Thermal variation of $\chi_M T$ of solvent exchanged samples of **2** measured in contact with the solvent. Empty circles: **2·PhCN**; full circles: **2·DMF**; red full circles: **2·MeOH** (a). Thermal variation of $\chi_M T$ of **2·PhCN**, **2·PhCN·MeCN** and **2·PhCN·MeCN·PhCN** (b).

Discussion about the magnetic properties and Mössbauer spectra of filtered samples.

$\chi_{\text{M}}T$ of filtered crystals of **2**·MeCN changes drastically with respect to the same sample measured in contact with the mother liquor. Thus, $\chi_{\text{M}}T$ shows a gradual increase from $2.4 \text{ cm}^3 \cdot \text{K} \cdot \text{mol}^{-1}$ (around 70 % HS fraction) to $2.9 \text{ cm}^3 \cdot \text{K} \cdot \text{mol}^{-1}$ at 300 K (around 80 % HS fraction from 50 to 300 K (see **Fig. S17**). A resolvated sample, obtained by soaking the filtered crystals of **2**·MeCN in MeCN, does not recover the spin transition shown by the solvated sample. Thus, $\chi_{\text{M}}T$ values higher than $3.3 \text{ cm}^3 \cdot \text{K} \cdot \text{mol}^{-1}$ are obtained at temperatures above 50 K indicating that the HS state fraction is close to 100 % (see **Fig. S17**). The different behavior of this resolvated sample with respect to the **2**·MeCN indicates that the structure of the initial sample is not completely recovered after resolution as shown by differences in the PXRD pattern (see above). Another factor that could explain this behavior is the cracking of the crystals into smaller crystallites after extracting them from the mother liquor, which could lead to the observed stabilization of the HS state in all the range of temperatures. Similar size effects have been reported in the literature for 1-bpp iron(II) complexes.¹³

Mössbauer spectroscopy measurements in a filtered sample of **2**·MeCN were performed to confirm the oxidation and spin states of Fe(II) in **2** since it was not possible to measure solvated samples due to technical reasons. These measurements show a HS fraction close to 60 % below 200 K, which is consistent with magnetic measurements. In all cases, characteristic spectra of HS or LS Fe(II) were obtained confirming that iron is not oxidized to iron(III) and the presence of a mixture of solvates with different spin states in the filtered samples (see **Figs. S18** and **S19**, **table S3**). The Mössbauer spectra (**Fig. S18**) taken at 200 K and below are fitted with three quadrupole doublets (**Table S3**). The doublet with lower isomer shift relative to metallic αFe at 298 K, IS, and lower quadrupole splitting, QS, (**Table S3**) is consistent with LS Fe^{II}.^{14,15} The doublets with higher IS and QS are typical of HS Fe^{II}. The presence of two doublets for HS Fe^{II} may be related to the presence of two phases with different solvation degree. The relative areas of the LS and HS doublets do not change significantly in the 4-200 K temperature range with the fraction of LS Fe^{II} being approximately 37%. If a spectrum of this same sample is taken in vacuum at room temperature, the spectrum accumulation starting after keeping the sample in vacuum at 295 K for one day, the fraction of LS Fe^{II} decreases down to approximately 17% (**Fig. S19**, **Table S3**). Most probably the sample is desolvated, which stabilizes the HS state. Furthermore, low temperature spectra of this sample indicate that no spin transition occurs in the 4-295 K temperature range.

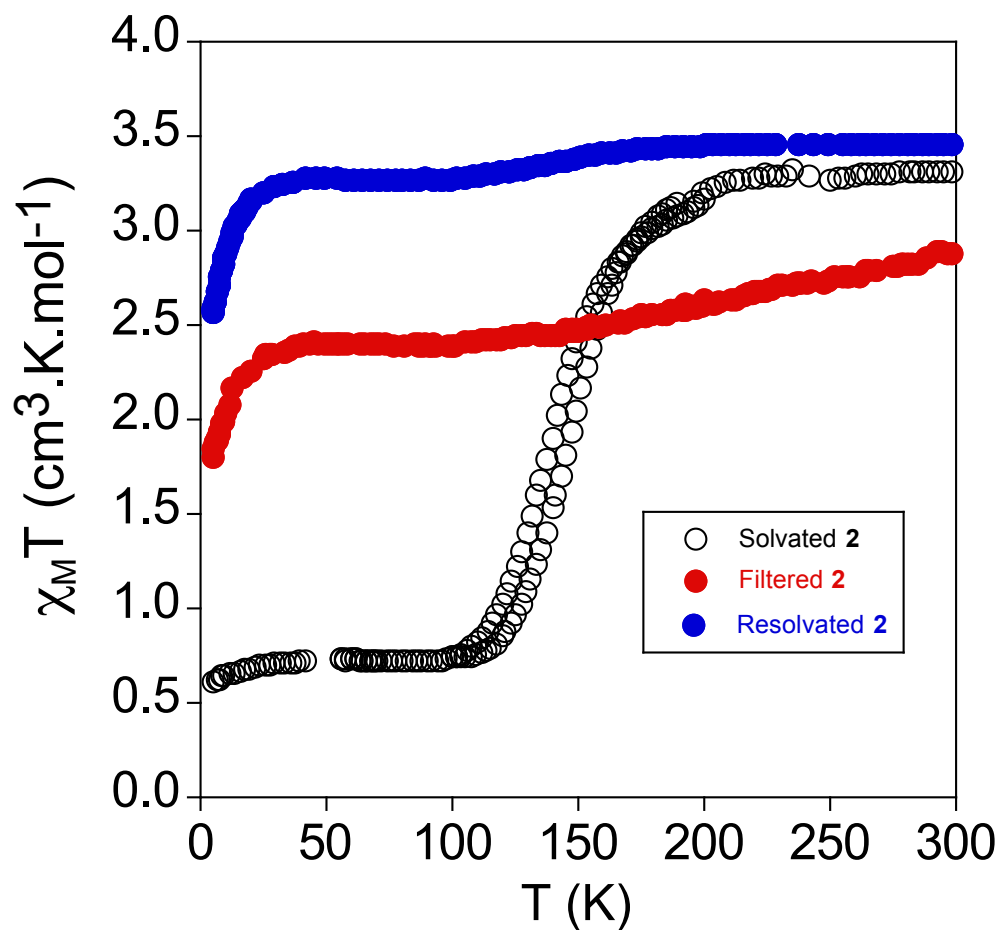


Fig. S17 Thermal variation of $\chi_M T$ of **2·MeCN**. Empty circles: Crystals in contact with the mother liquor; full red circles: Dried crystals after filtering; full blue circles: Dried crystals reimmersed in MeCN.

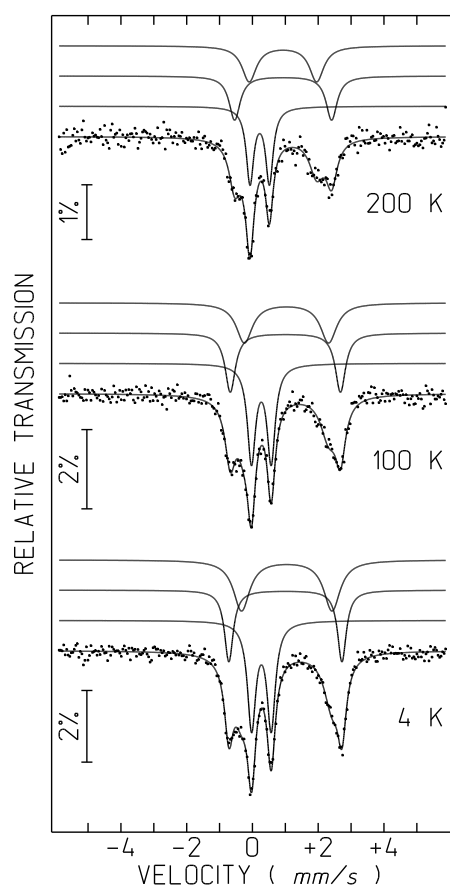


Fig. S18 Mössbauer spectra taken at different temperatures of freshly filtered crystals of **2**.

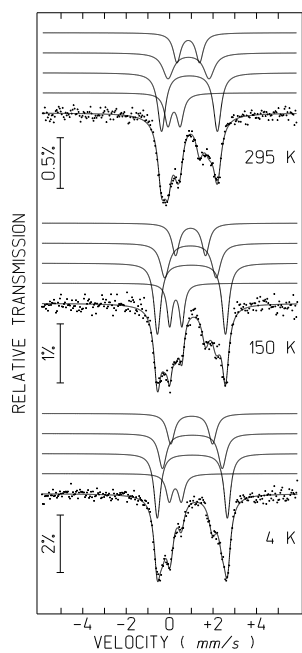


Fig. S19 Mössbauer spectra taken at different temperatures of **2** after being in vacuum for one day at 295 K.

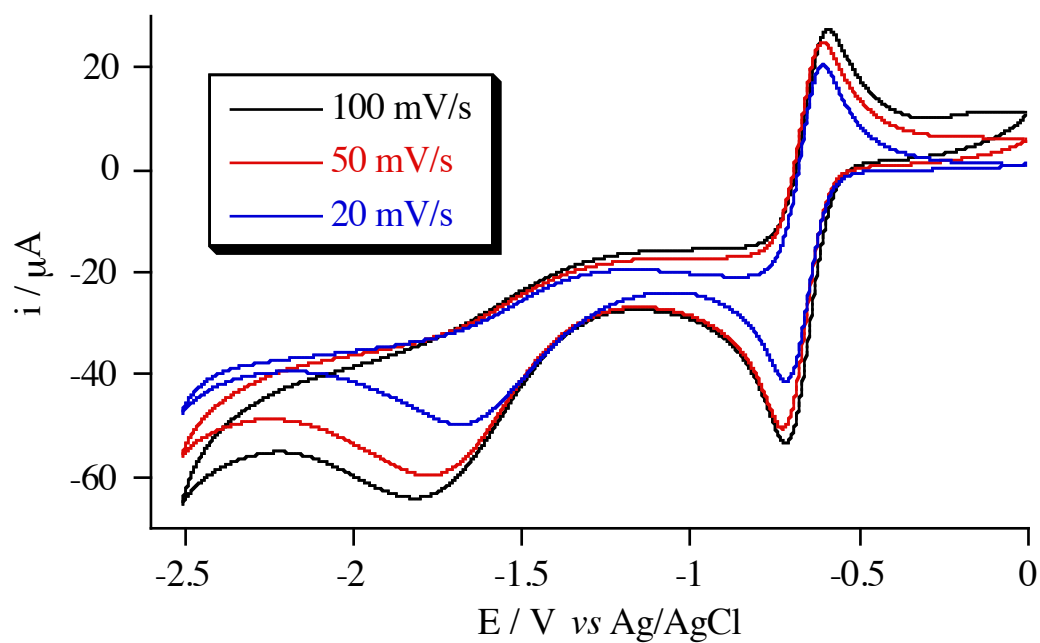
Table S3. Calculated parameters from the Mössbauer spectra of **2** taken at different temperatures T.

	T	IS	QS, ϵ	Fe ^{II} spin	I
Fresh filtered crystals of 2	200 K	0.33	0.59	LS	36%
		1.05	2.95	HS	31%
		1.04	2.05	HS	33%
	100 K	0.38	0.60	LS	38%
		1.11	3.35	HS	30%
		1.15	2.56	HS	32%
	75 K	0.39	0.60	LS	37%
		1.11	3.40	HS	30%
		1.15	2.66	HS	33%
	4 K	0.39	0.59	LS	38%
		1.11	3.44	HS	27%
		1.16	2.75	HS	35%
desolvated sample under vacuum at 295 K	295 K	0.31	0.56	LS	18%
		1.03	2.57	HS	39%
		0.98	1.89	HS	24%
		0.97	1.04	HS	19%
	150 K	0.40	0.55	LS	17%
		1.12	3.17	HS	39%
		1.08	2.33	HS	25%
		1.08	1.38	HS	19%
	4 K	0.37	0.55	LS	15%
		1.15	3.22	HS	38%
		1.16	2.75	HS	25%
		1.13	1.92	HS	21%

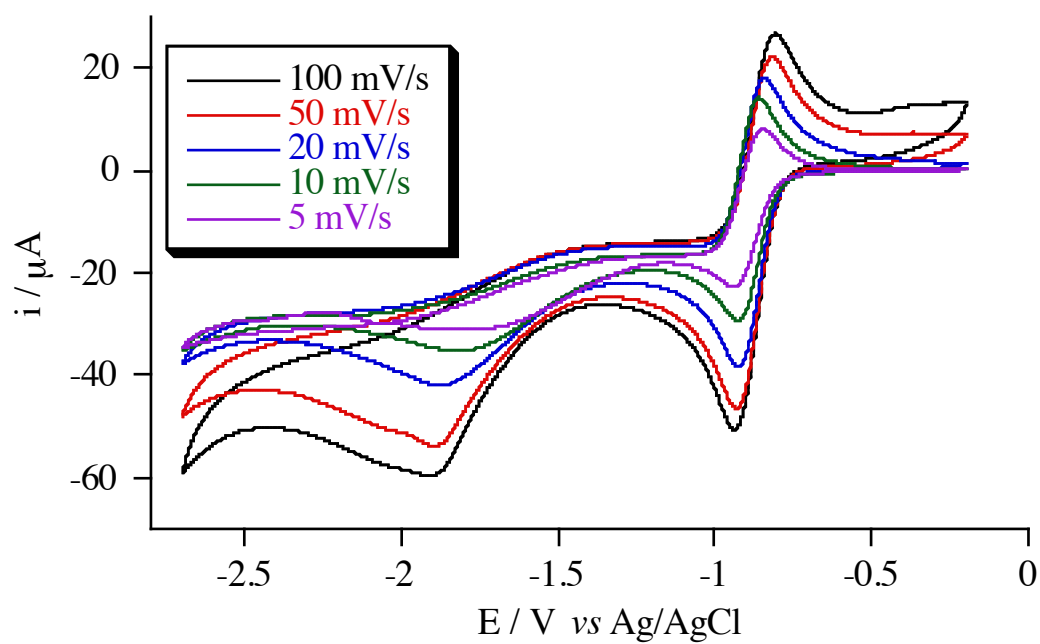
IS (mm/s) isomer shift relative to metallic α -Fe at 295 K; QS (mm/s) quadrupole splitting; I relative area. Estimated errors ≤ 0.02 mm/s for IS, QS, Γ and $<4\%$ for I.

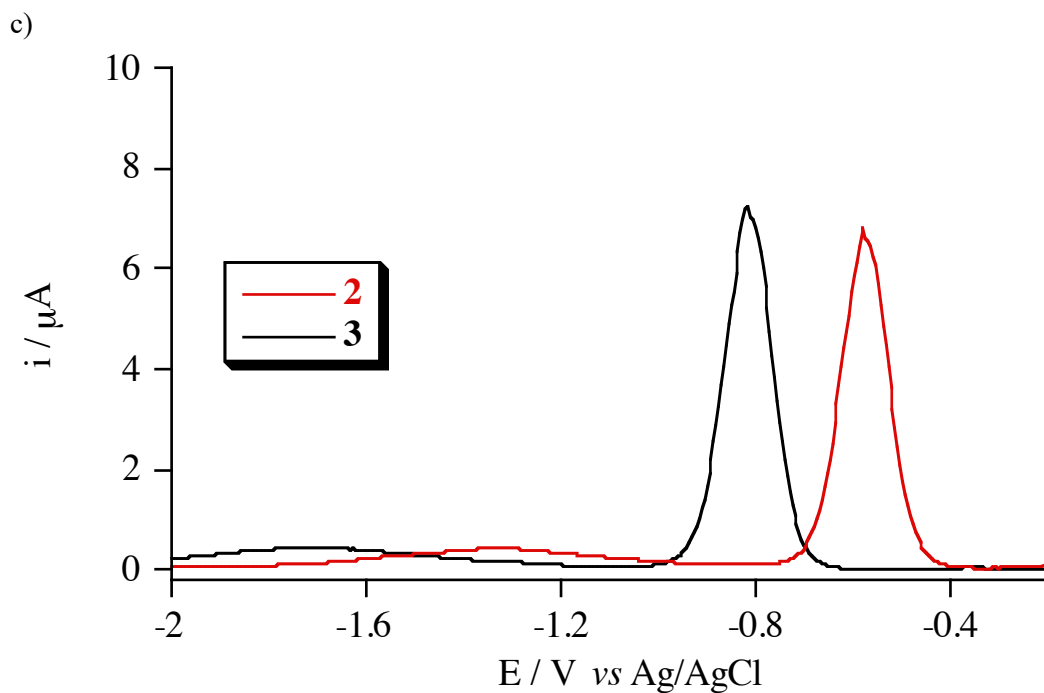
5. General characterization of Red 2, Red 3 and Reox 2.

a)



b)





d)

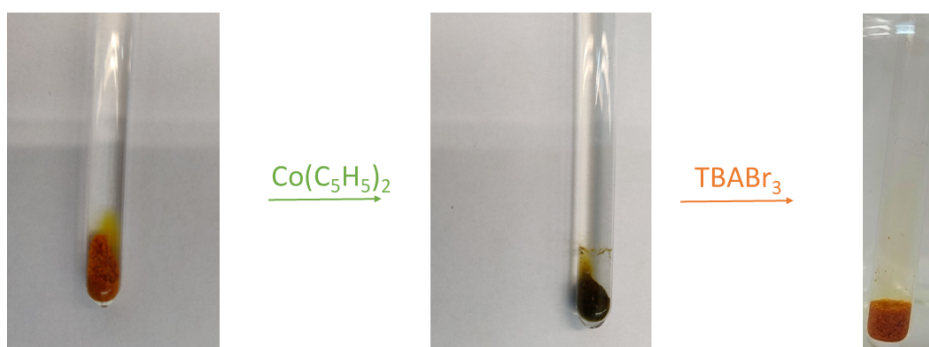


Fig. S20 Cyclic voltammetric behaviour of **2** (a) and **3** (b) and differential pulse voltammograms of **2** (red line) and **3** (black line) (c). Crystals of **2** (left) and **Red_2** (right) (d) Pictures of crystals of **2·MeCN**, **Red_2** and **Reox_2**.

Control experiments were performed soaking crystals of **3·MeCN** in ferrocene or dexamethylferrocenium tetrafluoroborate MeCN solutions. EDAX analysis of these samples indicated the absence of iron from ferrocene or dexamethylferrocenium. This confirms that reduction of hexavanadate by cobaltocene is a necessary condition for the entrance of cobaltocenium counteranions in the structure of **3**, since ferrocene, which is a weaker reducing agent,¹⁶ or dexamethylferrocenium, which is a cationic oxidant with a similar structure to that of cobaltocenium, do not enter in the structure in similar synthetic conditions.

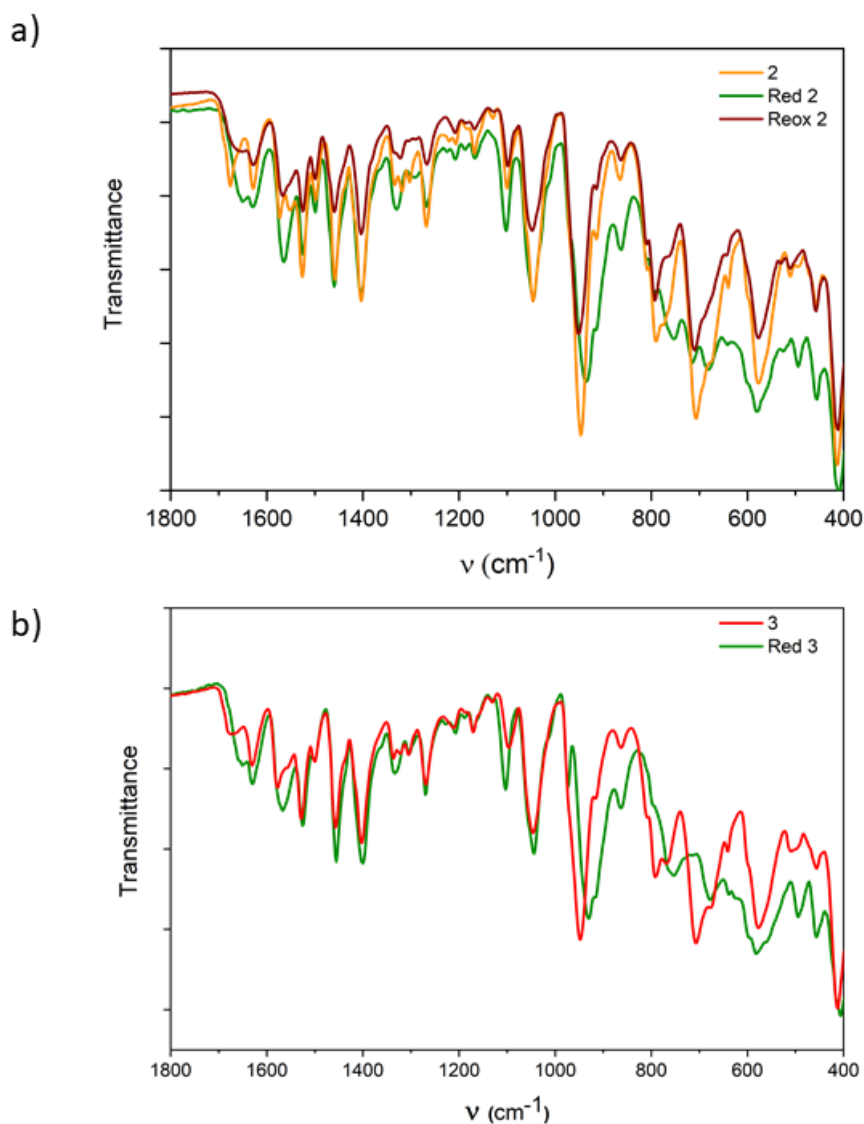


Fig. S21 (a) IR spectra of **2·MeCN**, **Red_2** and **Reox_2**; (b) IR spectra of **3·MeCN** and **Red_3**.

IR spectra of **2·MeCN** and **3·MeCN** show the characteristic stretching vibrations of the fully oxidized hexavanadate cage at ca. 950 cm^{-1} ($\nu\text{V}=\text{O}$) and 790 cm^{-1} ($\nu\text{V}-\text{O}-\text{V}$). These bands are shifted to a lower energy for **Red_2** and **Red_3** samples (ca. 930 cm^{-1} ($\nu\text{V}=\text{O}$) and 755 cm^{-1} ($\nu\text{V}-\text{O}-\text{V}$), see Fig. S21). These changes are reversible as these bands are again shifted to higher energies upon reoxidation in **Reox_2** sample (950 cm^{-1} ($\nu\text{V}=\text{O}$) and 790 cm^{-1} ($\nu\text{V}-\text{O}-\text{V}$), see Fig. S21). A similar trend has been reported in the stretching $\nu\text{V}=\text{O}$ band of fully alkylated hexavanadate derivatives. This has been attributed to the smaller positive charge on the vanadium atoms in the reduced species, which diminishes the polarity of the bonds to the respective terminal oxygen atoms thus shifting to lower frequencies upon reduction of the cluster.¹⁷ On the other hand, similar values of the $\nu\text{V}-\text{O}-\text{V}$ band upon reduction have been reported for coordination polymers formed by bis(pyridyl)-capped hexavanadate linked to divalent first-row transition-metal ions.¹⁸

High-resolution X-ray photoelectron spectroscopy (XPS) of **Red_2** and **Red_3** display two characteristic peaks at 780.7-781.4 ($2p_{3/2}$) and 795.6-796.3 ($2p_{1/2}$) eV from cobaltocenium. (Fig. **S22** and **S23**)¹⁹ The presence of cobaltocenium cations is further confirmed by ¹H NMR of filtered crystals of **Red_2** and **Red_3**, dissolved in dimethyl sulfoxide-*d*₆, which displays a singlet close to 5.9 ppm similar to that reported in literature for cobaltocenium (Fig. **S24**).²⁰ XPS spectra were also used to test the oxidation state of vanadium (see **Figs S22** to **S23**). Thus, high resolution XPS spectra of **2·MeCN** and **3·MeCN** present two characteristic peaks centered at 516.2 ($2p_{3/2}$) and 523.5 eV ($2p_{1/2}$) for **2·MeCN** and at 517.1 ($2p_{3/2}$) and 524.6 eV ($2p_{1/2}$) for **3·MeCN**, which are characteristic of V(V).²¹ XPS spectra of **Red_2** and **Red_3** show an increase of peak width indicative of a mixture of V(IV) and V(V), which could be fitted to a minor contribution at 515.3 ($2p_{3/2}$) for **Red_2** and at 516.2 ($2p_{3/2}$) for **Red_3**, assigned to V(IV), and to a major contribution at 516.5 ($2p_{3/2}$) for **Red_2** and at 517.3 ($2p_{3/2}$) for **Red_3**, assigned to V(V). These results are consistent with the reduction of the POM after chemical reduction, which can be inferred from EPR and magnetic data (see below).

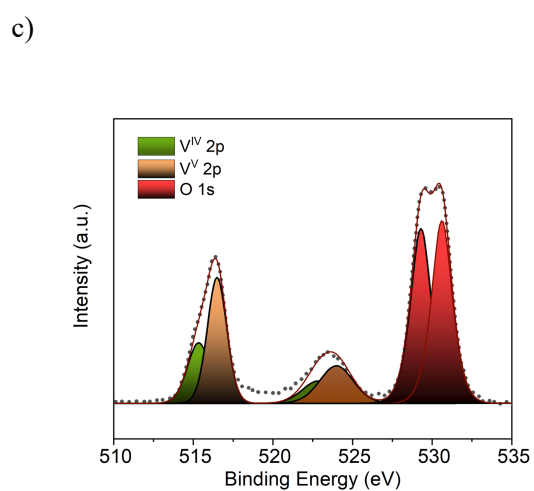
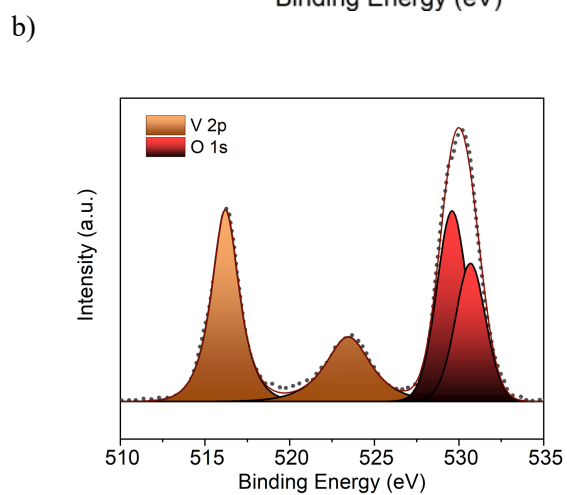
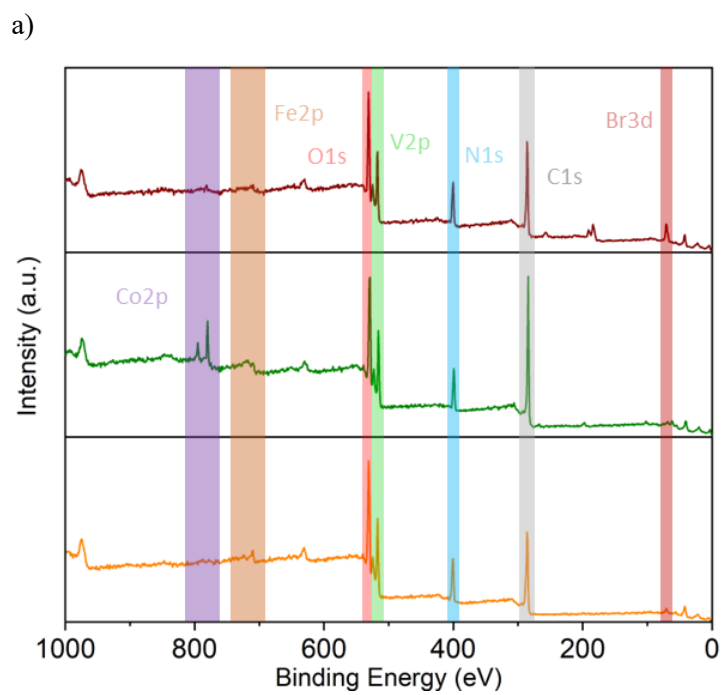


Fig. S22 XPS of **2-MeCN** (bottom), **Red_2** (middle) and **Reox_2** (top) (a), XPS V2p spectra of **2-MeCN** (b) and **Red_2** (c).

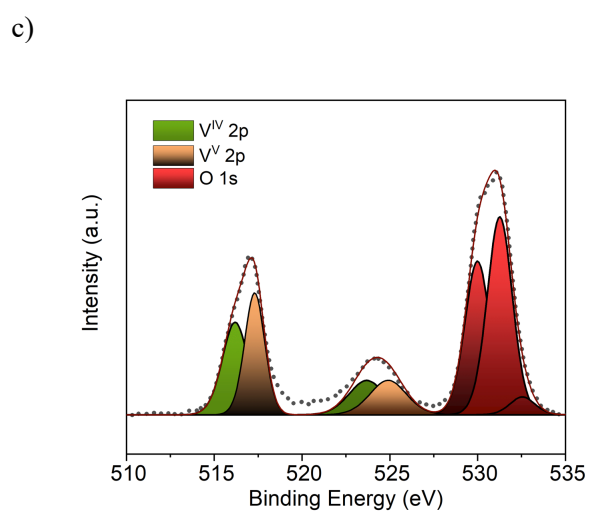
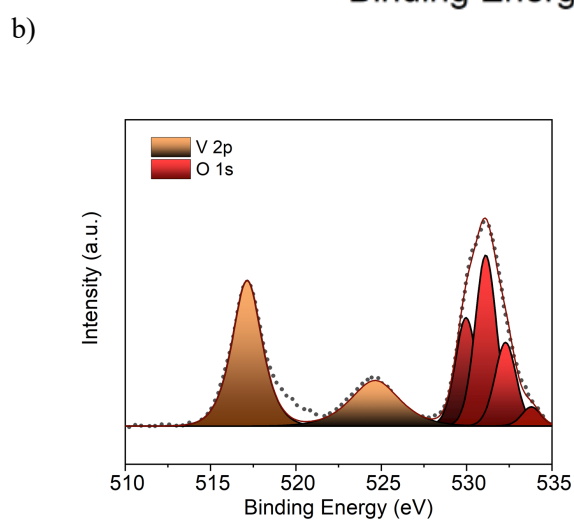
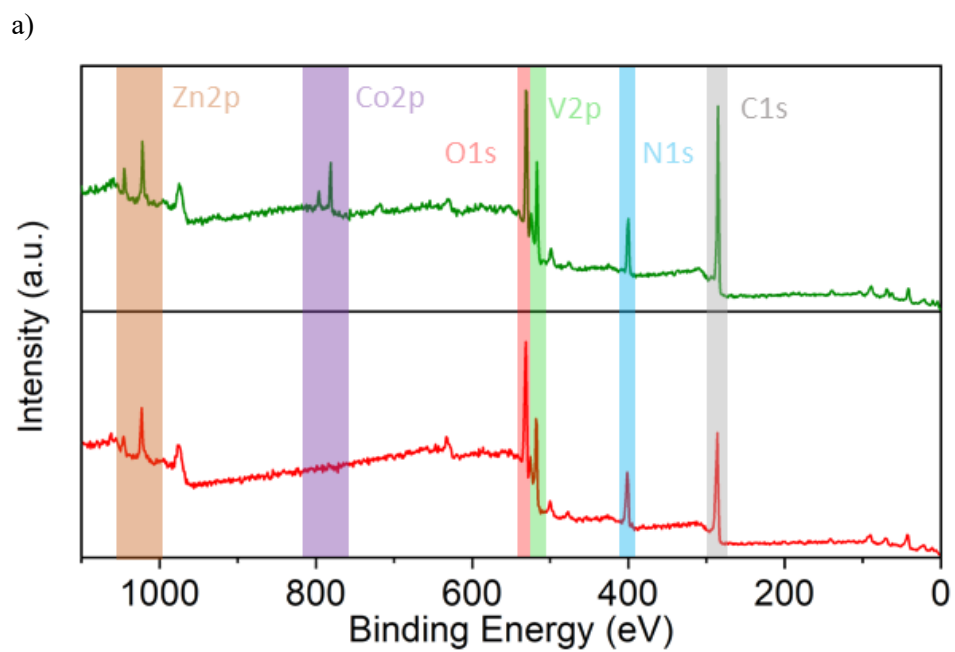
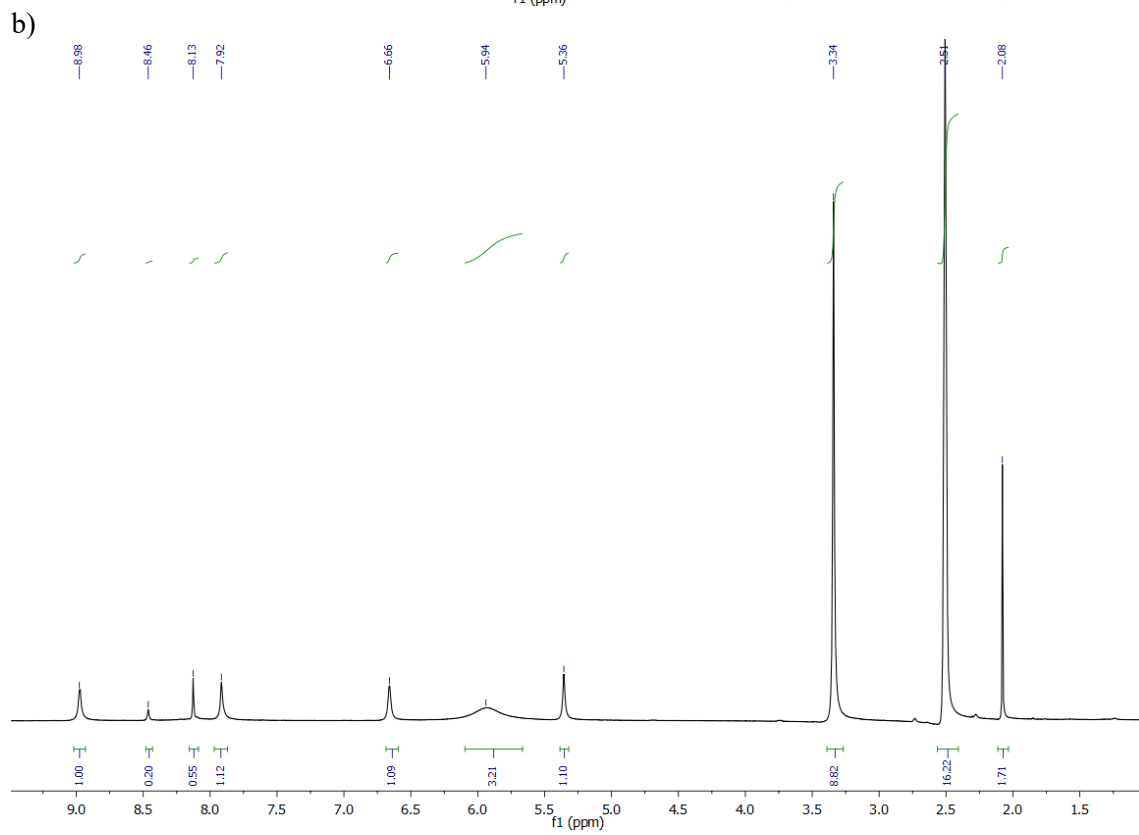
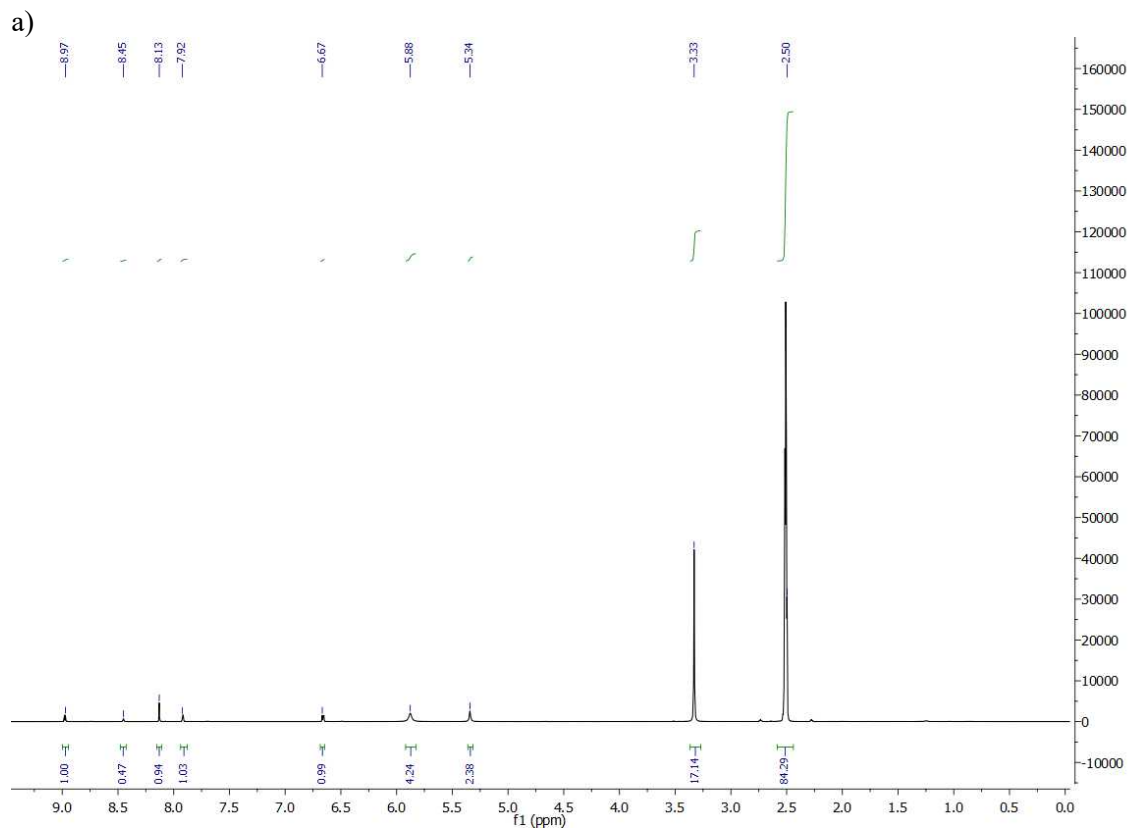


Fig. S23 XPS of **3·MeCN** (bottom) and **Red_3** (a), XPS V2p spectra of **3·MeCN** (b) and **Red_3** (c).



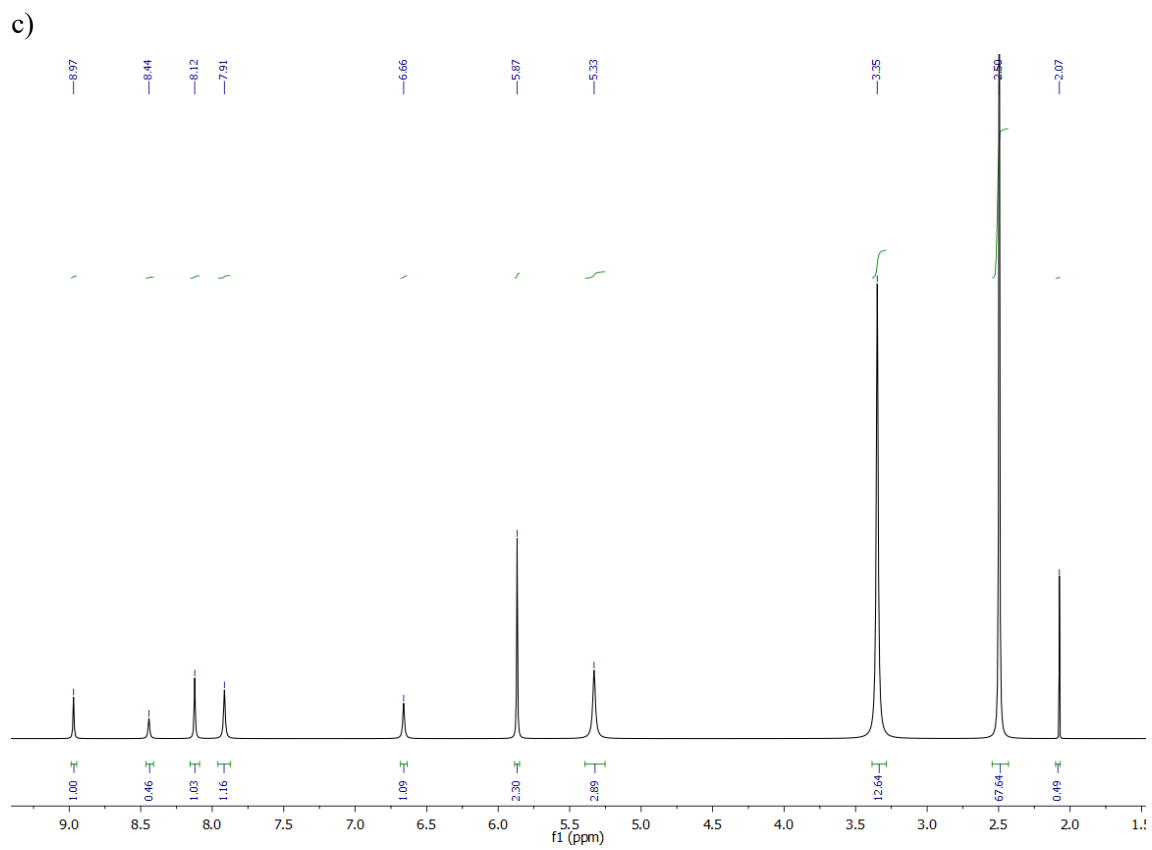


Fig. S24 ^1H NMR spectra of crystals of **Red_2** (a) **Red_3** (b) and **Reox_2** (c) in dimethyl disulfoxide- d_6

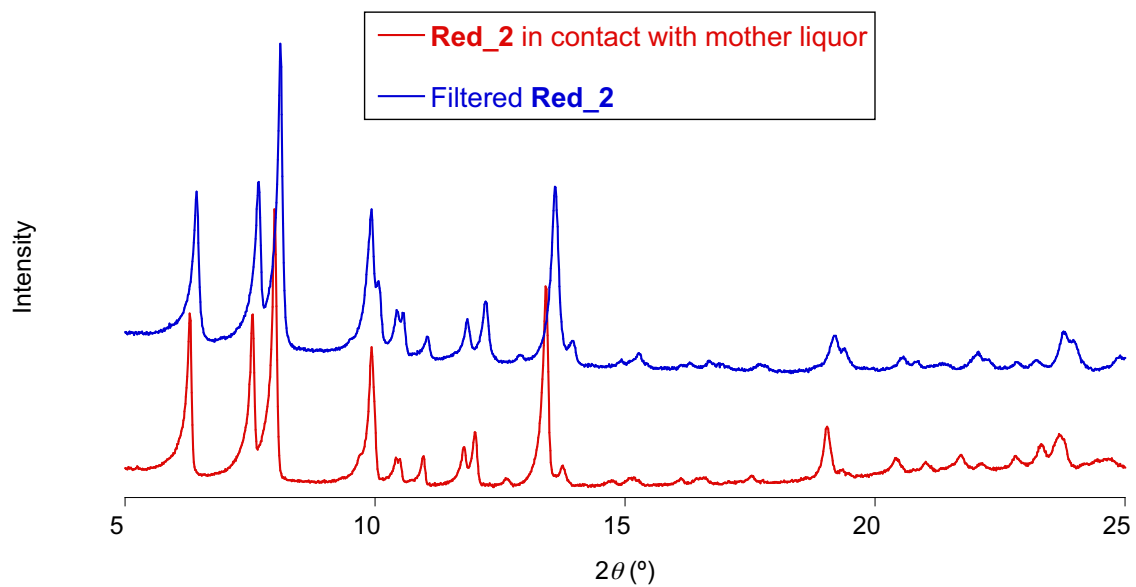


Fig. S25 PXR D patterns of **Red_2** measured in contact with the mother liquor (red line) and a dried sample of filtered crystals of **Red_2** (blue line).

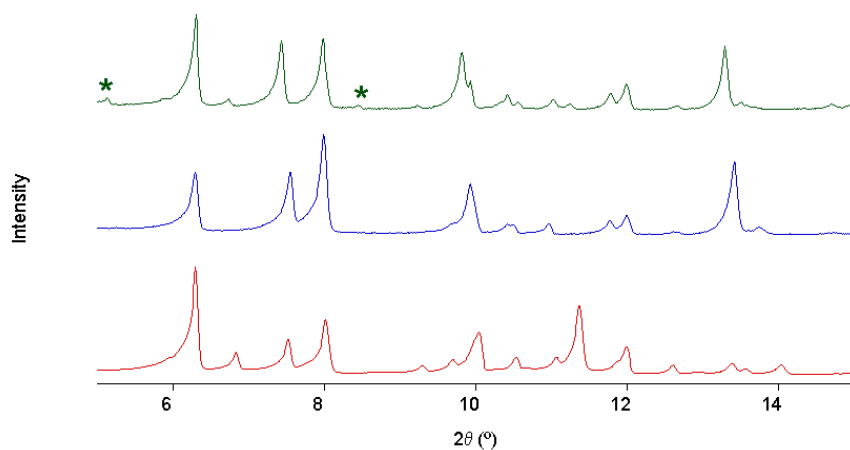


Fig. S26 PXRD patterns of **2·MeCN** (red line), **Red_2** (blue line) and **Reox_2** (green line) measured in contact with the mother liquor.

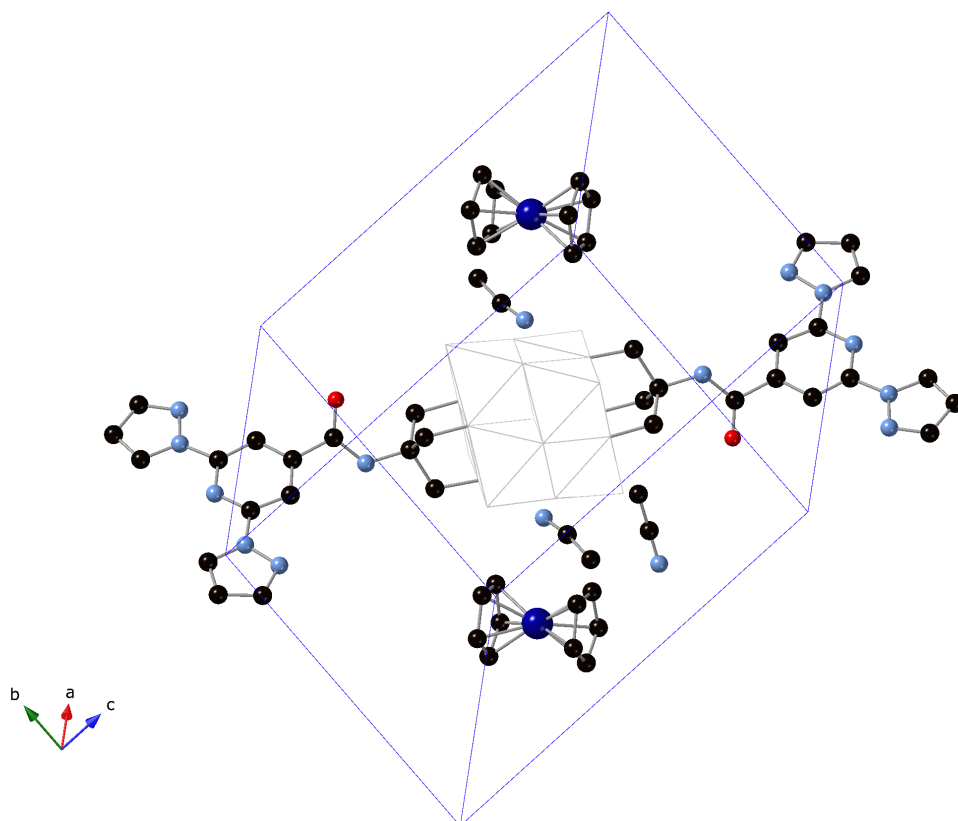


Fig. S27 Structure of $[\text{Co}(\text{C}_5\text{H}_5)_2]_2[\text{V}_6\text{O}_{19}(\text{C}_{16}\text{H}_{15}\text{N}_6\text{O})_2] \cdot \text{MeCN}$ (Co (dark blue), V (white), C (black), N (blue), O (red)). Hydrogen atoms have been omitted for clarity.

Red crystals of $[\text{Co}(\text{C}_5\text{H}_5)_2]_2[\text{V}_6\text{O}_{19}(\text{C}_{16}\text{H}_{15}\text{N}_6\text{O})_2] \cdot \text{MeCN}$ were obtained as a minority product from crystals of **Red_3** placed in a solution of TBABr_3 in MeCN for several days.

Table S4 Crystal data and structure refinement for $[\text{Co}(\text{C}_5\text{H}_5)_2]_2[\text{V}_6\text{O}_{19}(\text{C}_{16}\text{H}_{15}\text{N}_6\text{O})_2] \cdot \text{MeCN}$.

Empirical formula	$\text{C}_{30}\text{H}_{32}\text{CoN}_8\text{O}_{10.5}\text{V}_3$
Formula weight	884.38
Temperature/K	120.00(10)
Crystal system	triclinic
Space group	P-1
a/Å	9.8603(3)
b/Å	12.1228(4)
c/Å	17.2505(4)
$\alpha/^\circ$	79.422(2)
$\beta/^\circ$	80.163(2)
$\gamma/^\circ$	76.369(3)
Volume/Å ³	1952.25(10)
Z	2
$\rho_{\text{calc}}/\text{cm}^3$	1.504
μ/mm^{-1}	1.175
F(000)	896.0
Crystal size/mm ³	0.38 × 0.31 × 0.11
Radiation	MoK α ($\lambda = 0.71073$)
2 θ range for data collection/ $^\circ$	5.958 to 59.792
Index ranges	$-13 \leq h \leq 13, -16 \leq k \leq 16, -22 \leq l \leq 24$
Reflections collected	37801
Independent reflections	10216 [$R_{\text{int}} = 0.0538, R_{\text{sigma}} = 0.0601$]
Data/restraints/parameters	10216/3/476
Goodness-of-fit on F^2	1.058
Final R indexes [$I \geq 2\sigma(I)$]	$R_1 = 0.0729, wR_2 = 0.2192$
Final R indexes [all data]	$R_1 = 0.1093, wR_2 = 0.2514$
Largest diff. peak/hole / e Å ⁻³	1.95/-0.57

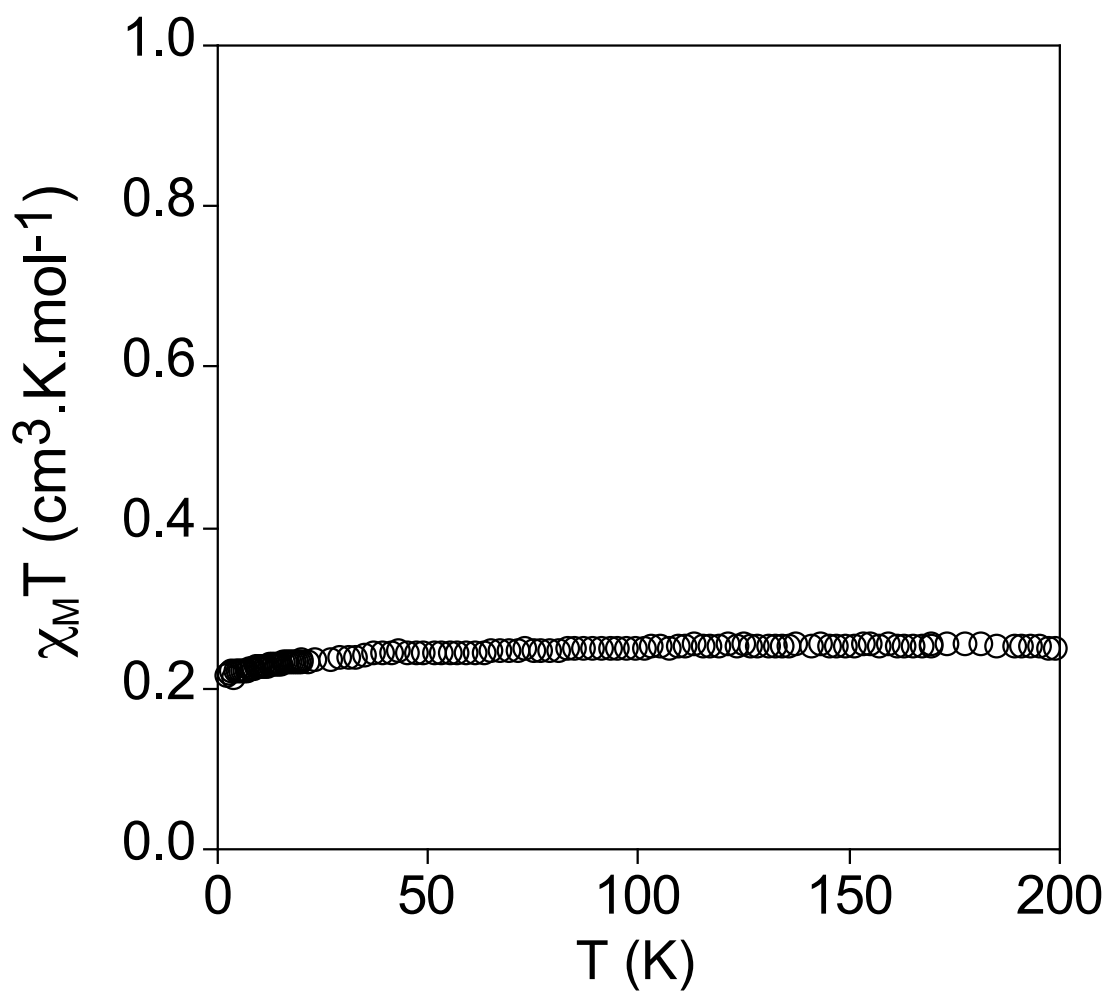


Fig. S28 Thermal variation of $\chi_M T$ of Red_3 measured in contact with the mother liquor.

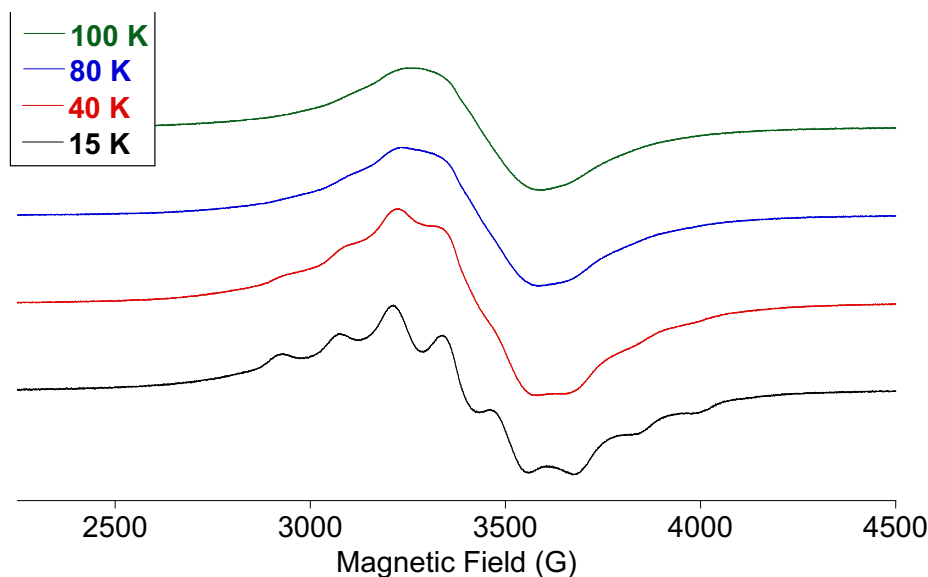


Fig. S29 EPR spectra of Red_3 measured in contact with the mother liquor.

EPR spectra are completely different to those of cobaltocene in diluted diamagnetic matrices²² confirming the absence of residual cobaltocene and the oxidation state III of the inserted cobaltocenium cations. This is confirmed by measurements of the filtered samples in contact with air, in which cobaltocene is not stable, which are similar to those of **2** and **3** samples measured in contact with the mother liquor.

6. References

- 1 V. W. Day, W. G. Klemperer and D. J. Maltbie, *J. Am. Chem. Soc.*, 1987, **109**, 2991-3002.
- 2 A. Abhervé, M. Palacios-Corella, J. M. Clemente-Juan, R. Marx, P. Neugebauer, J. van Slageren, M. Clemente-León and E. Coronado, *J. Mater. Chem. C*, 2015, **3**, 7936-7945.
- 3 G. M. Sheldrick, *Acta Crystallogr. Sect. A Found. Crystallogr.*, 2015, **71**, 3.
- 4 G. M. Sheldrick, *Acta Crystallogr. Sect. C Struct. Chem.*, 2015, **71**, 3.
- 5 O. V. Dolomanov, L. J. Bourhis, R. J. Gildea, J. A. K. Howard and H. Puschmann, *J. Appl. Crystallogr.*, 2009, **42**, 339.
- 6 G. S. Pawley, *J. Appl. Crystallogr.*, 1981, **14**, 357-361.
- 7 A. A. Coelho, TOPAS-Academic, Version 4.1, 2007, see <http://www.topas-academic.net>.
- 8 G. J. Long, T. E. Cranshaw and G. Longworth, *Mossb. Effect. Ref. Data J.*, 1983, **6**, 42.
- 9 J.C. Waerenborgh, P. Salamakha, O. Sologub, A.P. Gonçalves, C. Cardoso, S. Sérgio, M. Godinho and M. Almeida, *Chem. Mater.*, 2000, **12**, 1743-1749
- 10 M. P. Santoni, A. K. Pal, G. S. Hanan, A. Proust and B. Hasenknopf, *Inorg. Chem.*, 2011, **50**, 6737-6745.
- 11 Q. Chen, D. P. Goshorn, C. P. Scholes, X.-L. Tan and J. Zubieta, *J. Am. Chem. Soc.*, 1992, **114**, 4667-4681.
- 12 E. F. Wilson, H. N. Miras, M. H. Rosnes and L. Cronin, *Angew. Chem. Int. Ed.*, 2011, **50**, 3720-3724.
- 13 K. Senthil Kumar, B. Heinrich, S. Vela, E. Moreno-Pineda, C. Bailly and M. Ruben, *Dalton Trans.*, 2019, **48**, 3825.
- 14 P. Gütllich, Y. Garcia and H. A. Goodwin, *Chem. Soc. Rev.*, 2000, **29**, 419-427.
- 15 N. N. Greenwood, T. C. Gibb, "Mössbauer Spectroscopy" Chapman and Hall, Ltd. Publishers, London (1971).
- 16 N. G. Connelly and W. E. Geiger, *Chem. Rev.*, 1996, **96**, 877.
- 17 C. Daniel and H. Hartl, *J. Am. Chem. Soc.*, 2005, **127**, 13978.
- 18 J. W. Han, K. I. Hardcastle and C. L. Hill, *Eur. J. Inorg. Chem.*, 2006, **2006**, 2598.
- 19 (a) O. Henrion and W. Jaegermann, *Surf. Sci.*, 1997, **387**, L1073, (b) L. Zhang, N. Vilà, A. Walcarius and M. Etienne, *ChemElectroChem*, 2018, **5**, 2208.
- 20 (a) N. El Murr, *J. Organomet. Chem.*, 1976, **112**, 189; (b) I. E. Philip and A. E. Kaifer, *J. Am. Chem. Soc.*, 2002, **124**, 12678.
- 21 (a) J. K. Li, X. Q. Huang, S. Yang, H. W. Ma, Y. N. Chi and C. W. Hu, *Inorg. Chem.*, 2015, **54**, 1454; (b) X. Hu, Z. Xiao, B. Huang, X. Hu, M. Cheng, X. Lin, P. Wu and Y. Wei, *Dalton Trans.*, 2017, **46**, 8505
- 22 J. L. Robbins, N. Edelstein, B. Spencer and J. C. Smart, *J. Am. Chem. Soc.*, 1982, **104**, 1882.